2009

Characterization of Firn Microstructure Using Scanning Electron Microscopy: Implications for Physical Properties Measurements and Climate Reconstructions

Nicole Spaulding

CHARACTERIZATION OF FIRN MICROSTRUCTURE USING SCANNING ELECTRON MICROSCOPY: IMPLICATIONS FOR PHYSICAL PROPERTIES MEASUREMENTS AND CLIMATE RECONSTRUCTIONS

By

Nicole Spaulding

B.A. Colgate University, 2002

A THESIS

Submitted in Partial Fulfillment of the

Requirements for the Degree of

Master of Science

(in Quaternary and Climate Studies)

The Graduate School

University of Maine

August, 2009

Advisory Committee:

Debra A. Meese, Research Professor of Climate Studies, Advisor

Paul Mayewski, Professor of Earth Sciences and Climate Studies and

      Director of Climate Change Institute

Gordon Hamilton, Associate Professor of Climate Studies

Ian Baker, Professor of Engineering Dartmouth College

CHARACTERIZATION OF FIRN MICROSTRUCTURE USING SCANNING ELECTRON MICROSCOPY: IMPLICATIONS FOR PHYSICAL PROPERTIES MEASUREMENTS AND CLIMATE RECONSTRUCTIONS

By

Nicole Spaulding

B.A. Colgate University, 2002

A THESIS

Submitted in Partial Fulfillment of the

Requirements for the Degree of

Master of Science

(in Quaternary and Climate Studies)

The Graduate School

University of Maine

August, 2009

Advisory Committee:

Debra A. Meese, Research Professor of Climate Studies, Advisor

Paul Mayewski, Professor of Earth Sciences and Climate Studies and

      Director of Climate Change Institute

Gordon Hamilton, Associate Professor of Climate Studies

Ian Baker, Professor of Engineering Dartmouth College

THESIS
ACCEPTANCE STATEMENT

On behalf of the Graduate Committee for Nicole Spaulding, I affirm that this manuscript is the final and accepted thesis. Signatures of all committee members are on file with the Graduate School at the University of Maine, 42 Stodder Hall, Orono Maine.

Dr. Debra Meese, Research Professor of Climate Studies 08/14/09

THESIS
ACCEPTANCE STATEMENT

On behalf of the Graduate Committee for Nicole Spaulding, I affirm that this manuscript is the final and accepted thesis. Signatures of all committee members are on file with the Graduate School at the University of Maine, 42 Stodder Hall, Orono Maine.

Dr. Debra Meese, Research Professor of Climate Studies 08/14/09
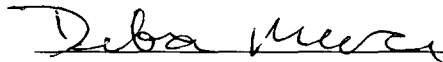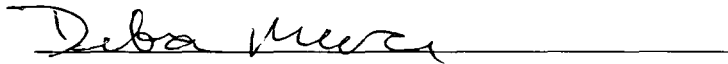
THESIS
ACCEPTANCE STATEMENT

On behalf of the Graduate Committee for Nicole Spaulding, I affirm that this manuscript is the final and accepted thesis. Signatures of all committee members are on file with the Graduate School at the University of Maine, 42 Stodder Hall, Orono Maine.

Dr. Debra Meese, Research Professor of Climate Studies 08/14/09

LIBRARY RIGHTS STATEMENT

In presenting this thesis in partial fulfillment of the requirements for an advanced degree at The University of Maine, I agree that the Library shall make it freely available for inspection. I further agree that permission for "fair use" copying of this thesis for scholarly purposes may be granted by the Librarian. It is understood that any copying or publication of this thesis for financial gain shall not be allowed without my written permission.

Signature: *Nicole Spaulding*

Date: 08 | 14 | 09

CHARACTERIZATION OF FIRN MICROSTRUCTURE USING SCANNING ELECTRON MICROSCOPY: IMPLICATIONS FOR PHYSICAL PROPERTIES MEASUREMENTS AND CLIMATE RECONSTRUCTIONS

By Nicole E. Spaulding

Thesis Advisor: Dr. Debra A Meese

An Abstract of the Thesis Presented
in Partial Fulfillment of the Requirements for the
Degree of Master of Science
(in Quaternary and Climate Studies)
August, 2009

Samples from 12 East Antarctic firn and ice cores were analyzed using scanning electron micrcoscopy (SEM) in order to first develop a technique for the accurate characterization of physical properties and then to investigate the relationship between the physical microstructure and chemical properties. Both physical properties, such as grain size and porosity, and chemical properties, such as major ion and trace element concentration, provide information about atmospheric temperature changes, impurity content, accumulation rate and deformation history; therefore the characterization of both types of properties is necessary. Further, knowledge of the relationship between the physical and chemical properties may increase our ability to interpret paleoclimate proxies.

Using samples for which grain size measurements based on traditional methodologies (*Gow*, 1969; *Gay and Weiss*, 1999) existed, new grain sizes were calculated using images from SEM. Unlike previous methodologies, SEM samples do

not require the use of pore filler. Measurements from SEM were found to be smaller than those calculated using traditional methodologies. These differences were attributed to the increased accuracy of the new technique resultant from the visibility of clear etched grain boundaries and open pores. The newly calculated grain sizes were used to calculate an updated activation energy. These calculations revealed that although SEM measurements of grain size are smaller, especially for grain smaller than 0.4 mm^2, the difference is not great enough to invalidate the previously established Arrhenius type temperature dependence of grain growth.

The physical and chemical microstructures were characterized using SEM and X-ray micro-computed tomography in four East Antarctica cores at three depths (30, 60, 90 m) in order to assess the relationship between the chemical and physical properties. Physical properties characterization (grain size, porosity, density, internal surface volume, and crystallographic orientation) revealed expected differences between sites 06-1 and 07-4, resultant from differences in the moisture content and accumulation rate at their respective locations, as well as some unexpected findings. Indications of shallow subgrain formation and trends in internal surface volume which have implications for the study of firn densification were found. Orientation patterns suggested the c-axis ({0001} plane) as the primary axis of rotation, resultant from the weight of overlying ice. Chemical characterization revealed that site specific differences in aerosol and particulate concentration and source between sites 06-1 and 07-4 could accurately be determined using EDS analysis. It was also found that the combination of elements predominant within the sample controls the morphology and microstructural location of the impurities.

ACKNOWLEDGEMENTS

TABLE OF CONTENTS

LIST OF TABLES

Chapter 1

INTRODUCTION

1.1 ICE SHEET FORMATION

Ice sheet formation occurs when, for an extended period of time, the amount of snow lost to melting and evaporation is less than the amount of snow deposited in the same area. Snow that remains on the ground after a summer season becomes more dense with the reduction of pore space as grains make contact and material is transferred from one grain to another (sintering). Grain growth is then driven by the minimization of grain boundary area which further reduces pore space. At this stage the material is referred to as *firn*. As firn becomes buried deeper and deeper in the ice sheet with continued accumulation, the increased pressure of overlying snow results in larger more aggregated grains that combined create a material of still higher density. Eventually, the pore space becomes so reduced and unconnected that the air space between particles is closed off and the material is considered ice around a density of ~ 0.84 g/cm^3.

1.2 ICE CORE CLIMATE RECONSTRUCTIONS

Each layer of snow that is successively buried contains within it aerosol and particulate impurities that provide information about the atmospheric chemistry and circulation at the time of deposition. Some chemical species exhibit very strong seasonal cycles. For example, Na$^+$, a sea salt tracer, has a strong winter maxima that is related to more frequent advection of marine air masses over the continent in winter. Increases in dust species can be related to warmer and windier conditions (*Legrand and Mayewski*, 1997). In addition, the physical structure can indicate the temperature at which the ice was formed and records deformation resulting from stresses and strains within the ice

1

sheet, including ice flow. Therefore, firn and ice can be used to reconstruct long-term records of climate using cores extracted from the ice sheet using a drilling apparatus. Many ice cores have been collected by the International Trans-Antarctic Scientific Expedition (ITASE) in order to identify the spatial and temporal resolution of climate records in Antarctica over the last approximately 200 years. The ice cores used in this study were collected by the U. S. component of that program.

Preparation of ice cores for analysis typically involves melting the core and collecting discrete samples. The newest procedure for continuous melting with discrete sampling is described in *Osterberg and others* (2006). Analysis of the meltwater samples involves the determination of the isotopic and chemical composition. Gas source mass spectrometry is used for stable isotope analyses ($\delta^{18}O$ and δD). Ion exchange chromatography and inductively coupled plasma mass spectrometry are used to determine the concentration of major ions and trace metals, respectively. Both of these analytical techniques require melted samples and therefore physical measurements, such as grain size and porosity, cannot be made on the ice from which the discrete samples are collected.

1.3 PHYSICAL AND CHEMICAL CHARACTERIZATION OF ICE CORES

Scanning electron microscopy (SEM) and associated equipment provide characterization of both the physical and chemical structure of firn and ice samples. Calculations of physical parameters, such as grain size and percent areal porosity, can be made using images captured in SEM and chemical and crystallographic analysis can be conducted both during and after imaging.

In this study firn and ice samples were imaged using SEM with a secondary electron detector. In this technique, the primary electron beam is scanned across the surface of the sample causing electrons of a wide range of energies to be emitted from the surface in the region where the beam is incident. These electrons include backscattered primary electrons and Auger electrons, but the vast majority are secondary electrons. The secondary electron current reaching the detector is recorded and the microscope image consists of a "plot" of this current against probe position on the surface. The contrast in the micrograph arises from several mechanisms including composition and electrical conductivity, but primarily from variations in the surface topography (*Goldstein and others*, 1992). The resulting image illustrates the true surface structure.

Several analytical instruments were used in conjunction with SEM. The elemental chemistry of the impurities present was determined using energy dispersive X-ray spectroscopy (EDS) in association with SEM. EDS is a technique in which the interaction of the electron beam with the atoms of the impurity results in the emission of photons having a characteristic energy dependent upon the atoms from which they were produced (*Goldstein and others*, 1992).

Electron backscatter diffraction patterns (EBSPs) were used to characterize the crystallographic orientation of the grains allowing for an assessment of the deformation history. The formation of EBSPs results from the inelastic scattering of a fraction of the electrons with a small loss of energy to form a divergent source of electrons close to the surface of the sample. Those electrons which are incident on atomic planes at angles which satisfy the Bragg equation ($n\lambda = 2\,d\,\sin\theta$, where n is an integer, λ is the wavelength of the electrons, d is the spacing of the diffracting plane, and θ is the angle of

incidence of the electrons on the diffracting plane) are diffracted to form a set of paired large angle cones corresponding to each diffracting plane. The regions of enhanced electron intensity between the cones produce the characteristic Kikuchi bands of the electron backscatter diffraction pattern (*Oxford Instruments PLC*, 2005).

1.4 APPLICATION TO RESEARCH QUESTIONS

In chapter two of this thesis the true surface topography images captured by the SEM are used to evaluate a new method of grain size measurement. In the third chapter of this thesis the ability to characterize both chemical and physical parameters within a single sample is utilized in a suite of cores with a wide spatial and temporal range in order to investigate the relationship between the physical and chemical properties within firn and ice cores.

A NEW TECHNIQUE FOR FIRN GRAIN SIZE MEASUREMENTS USING SEM IMAGE ANALYSIS

2.1 INTRODUCTION

Firn and ice cores, such as those collected by the International Trans Antarctic Scientific Expedition (ITASE) (*Mayewski*, 1996; *Mayewski and others*, 2006), contain information about the soluble, insoluble and gaseous components of the atmosphere, as well as indicators of temperature, precipitation, atmospheric circulation, sea ice extent and volcanic activity (*Legrand and Mayewski*, 1997). Microstructural parameters, including grain size and porosity, provide additional information about atmospheric temperature changes, impurity content, accumulation rate and deformation history. Therefore, accurate measurements of grain size and porosity allow for the identification of layers that do not exhibit normal grain growth with depth, and the detection of anomalous changes in any of the factors affecting the growth and sintering of firn and ice grains i.e. impurity concentration, grain boundary pinning, stress and strain conditions, recrystallization, annealing, deformation and recovery. Spatial variations in microstructure provide insights into micro-meteorological conditions such as snow accumulation and wind patterns (*Rick and Albert*, 2004) that potentially affect the preservation of paleoclimate records. In addition, the microstructure of near-surface firn influences the reflection of electromagnetic radiation thereby affecting remote sensing and radar studies (e.g., *Zwally*, 1977; *Surdyk*, 2002).

Despite the importance of firn microstructure to paleoclimate reconstructions, little progress has been made in the measurement of firn grain size. The original method

of grain size measurement (*Gow*, 1969) used the average of the shortest and longest axes of the 50 largest grains as measured with a pocket comparator (a hand held magnification tool for making linear measurements). *Alley* (1980) modified this method slightly by excluding the five largest grains in the sample. Subsequent methods evolved to counting all grains within a known area (*Duval and Lorius*, 1980) or using the linear intercept method which expresses grain size as an average length by counting the number of grain boundary intersections along a known length (*Thorsteinsson and others*, 1995; *Alley and Woods*, 1996). A newer method uses digital images of thin-sections,and automated outlining and pixel counting software to derive grain size as a mean cross-sectional area (*Gay and Weiss*, 1999). These techniques which were developed to measure grains of all sizes, have seen only limited use in the study of firn as a result of the difficulty involved in processing firn samples.

The differences between the above techniques represent attempts to resolve the two primary sources of uncertainty in the estimation of grain size: how to calculate and report "size", and how to account for the cut effect and the intersection probability effect (*Higgins*, 2000). Both uncertainties arise from measuring an irregular three-dimensional structure using a two-dimensional image. The first source is a matter of determining which parameter (length or area) is most closely related to grain volume. The latter source results from the act of sectioning. When a thin-section is created it is unknown at which point and in how many places each grain has been cut. The plane from which average grain size is calculated will include cross sections ranging from small grain tips to the maximum grain diameter. Thus a range of sizes will be found even for a homogeneously-sized population: the so-called cut effect. An additional source of

uncertainty arises because smaller crystals are less likely to be intersected by the plane: the intersection probability effect (*Higgins*, 2000).

Each of the techniques discussed above has unique problems as well as common disadvantages. Traditional methods of grain size measurement in firn (e.g., *Gow*, 1969; *Duval and Lorius*, 1980; *Alley and Woods*, 1996; *Gay and Weiss*, 1999; and others) require the use of a pore filler (e.g., aniline or dodecane) because of the fragile nature of firn. The pore filler, despite its utility, obscures details of the microstructure, making accurate measurements difficult. This problem can be mitigated by using scanning electron microscopy (SEM). The SEM imaging technique of *Baker and others* (2007) provides high-resolution images of both grain and pore structure with minimal sample preparation. Because it requires no pore filler, SEM analysis allows visualization of both grain and pore geometry. This imaging technique is used in combination with a new measurement technique, described in this paper, to eliminate most of the uncertainties of past measurement techniques. A comparison between grain size measurements, growth rates and apparent activation energies calculated using this method and earlier methods reveals a number of differences, our analysis of these differences has implications for paleoclimate reconstructions using ice cores.

2.2 METHODS

There is considerable confusion surrounding the definitions of crystals and grains. *Gow* (1969) defines a grain as a unit having up to three crystals. The crystals within a grain are distinguished by changes in birefringence under crossed-polarizers. In materials science, polycrystalline materials are made up of individual grains each of which is a single crystal. These variations in terminology have resulted in confusion between fields.

The term grain, as used here, is in line with the materials science definition. We use this definition because visibly etched boundaries which typically align with a change in axis orientation (*Baker and others*, 2005; *Obbard and others*, 2006; *Sieg*, 2008) can be seen clearly in SEM images.

Grain size measurements from three firn and ice cores (02-1, 02-4, and 02-SP) collected during the 2002 US ITASE traverse in East Antarctica (Fig. 2.1) were derived using the techniques of *Gow* (1969), *Gay and Weiss* (1999) and a new technique described below. Samples were taken at those depths from which high quality digital thin-section photographs existed and enough sample remained to prepare an SEM specimen. Several cores were used in order to span the range of depths desired. For the first two techniques thin-section samples were photographed under crossed-polarizers with both a film camera and a digital camera (Fig. 2.2). The photographs were used to calculate grain size (*Gow and others*, 2004) using the methods of *Gow* (1969). These data are referred to as "GOW". The digital images were analyzed using the Image Pro Plus 5.0© software package which automatically outlines grains (as differentiated by birefringence patterns-Fig. 2.2b) and counts the pixels within each grain (Gay and Weiss, 1999). These samples are referred to as "G&W".

Our new technique entails the examination of SEM specimens using a Field Emission Gun (FEI) XL30 SEM operated at 15 kV with a beam current of 0.15 nA. Samples were maintained at -110°C ± 5°C using a custom-designed liquid nitrogen chilled cold stage (*Baker and others*, 2007). For each sample, a series of slightly overlapping secondary electron images were collected and digitally stitched together to form a mosaic of the horizontal surface of the sample (Fig. 2.3a). Grain sizes were
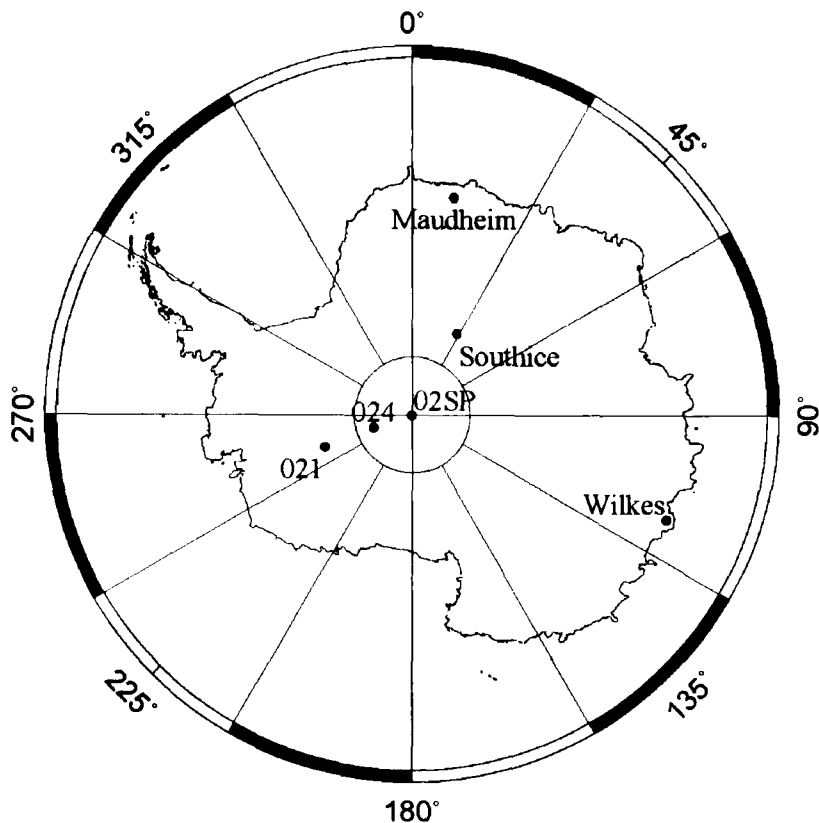
FIGURE 2.1. Map of core sites. Ice cores 02-1, 02-4, and 02-SP were used in this study to calculate grain sizes and growth rates. Maudheim, Southice, Wilkes, and two locations not shown (Site 2, Greenland and South Pole) were used in Fig. 2.4.

determined by manually tracing grain boundaries using Image Pro Plus 5.0© to create a skeleton outline of the boundaries (Fig. 2.3b). A pixel counting utility was applied to the skeleton outline to determine the grain area. These samples are referred to as "SPLD".

We adopt the practice of reporting mean grain size as a cross-sectional area based on all grains in the section for several reasons. A computer simulation of normal grain growth by *Anderson and others* (1989) indicates that using the mean cross-sectional area of all grains in the section is the combination of parameters most likely to eliminate the

9
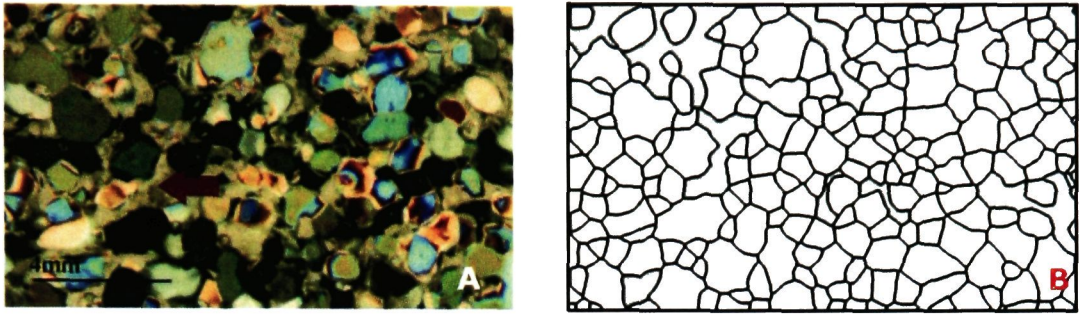
FIGURE 2.2. a) Thin section 02-1 16m under crossed-polarizers. Red arrow points to pore filler used in the preparation of thin-sections, which obscures the microstructure. b) Skeleton outline of grains. Gray portions indicate areas were pore filler has overlapped grains enough to obscure their shape. Outlines have been thickened for visibility at this scale. The two large grains to the left and immediately above the red arrow illustrate the "cut-effect". These grains appear larger than all the others and all the grains in Figure 2.3 because they were likely intersected at their widest point.
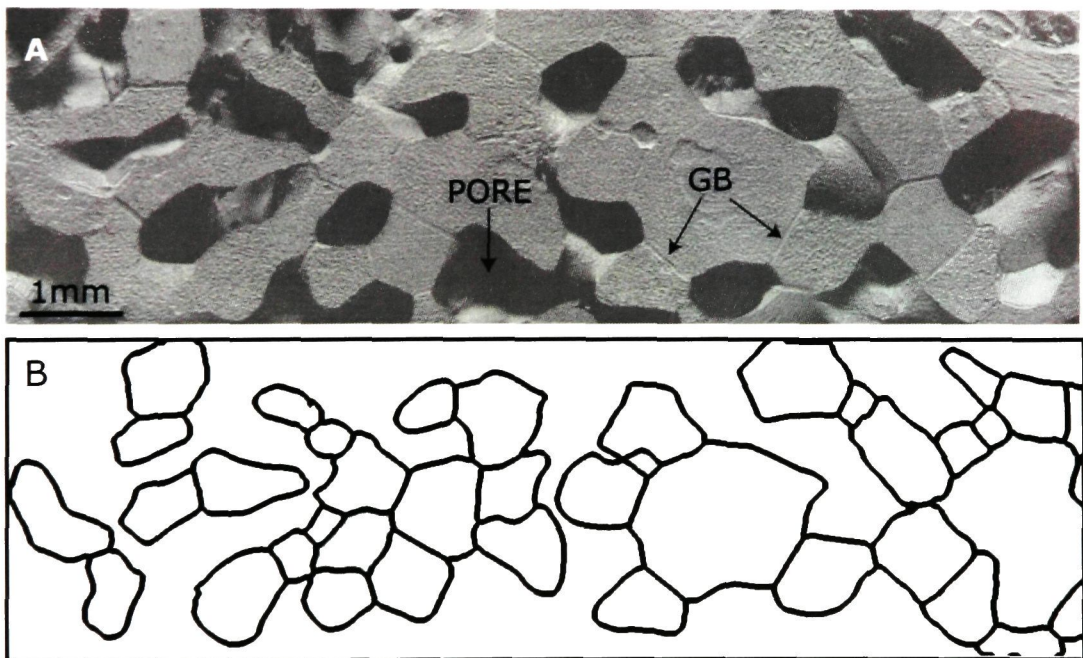
FIGURE 2.3. a) SEM image of 02-1 16m. SEM images require no pore filler and therefore most aspects of the microstructure are clearly visible. Prominent features such as pores and clearly etched grain boundaries (GB) which aid in the identification of individual grains are labeled. b) The skeleton outline of grain boundaries. Pores that are fully bound by grains have been colored gray. Boundary thickness has been amplified for ease of visibility.

uncertainties of the cut effect and the intersection probability effect. In their model, grains greater in size than the average grain size (as derived using all grains in the section) grew, whereas those smaller than the average grain size shrank. These model results indicate that mean grain size obtained using all grains in the section has a particular physical significance, which is not the case for only the largest grains. *Anderson and others* (1989) also noted the similarity in grain growth kinetics derived from mean grain volume with those based on mean grain cross-sectional area when grain morphology was consistently compact and the surface area to volume ratio was minimal.

2.3 RESULTS AND DISCUSSION

2.3.1 Grain Size

Grain size is a function of both age/depth and temperature (*Stephenson*, 1967; *Gow*, 1969). The linear relationship between age and mean grain cross section is:

$$\overline{A} = \overline{A}_0 + Kt$$

where $\overline{A}$ is the measured mean cross-sectional area (mm^2) at time t, $\overline{A}_0$ is the extrapolated mean cross-sectional area at t = 0, and K is the rate of grain growth. The equation rests on the assumption that growth rate is controlled by interfacial tension at the grain boundaries (*Cole and others*, 1954). The temperature dependence of K is described by the Arrhenius type equation:

$$K = K_0 \exp(-E_a / RT)$$

where T is temperature in Kelvin, K_0 is an empirical constant and E_a and R are the activation energy of grain boundary self diffusion and the gas constant, respectively. E_a is determined by the slope of the temperature grain growth (T-K) curve. This type of

dependence is appropriate because the ratio of the activation energy of grain boundary self-diffusion to volume self diffusion (determined experimentally) for ice (~6:10) is similar to that for most metals (*Gow and others*, 2004).

Grain sizes calculated using the three different techniques described above are plotted against depth for each core in Fig. 2.4. As expected, grain size increase with depth. Correlation coefficients were computed between grain size and depth for each method. The highest correlation between size and depth was for GOW samples (0.86), followed by SPLD (0.66) and G&W (0.48), indicating that site to site variations in grain size are masked by including only the 50 largest grains. There are additional reasons for the differences in correlation, as discussed below.

Comparison of the three techniques applied to samples from the 02-1, 02-4, and 02-SP cores revealed average grain sizes from SEM ($\overline{G}$ SPLD) to be significantly smaller than $\overline{G}$ GOW and $\overline{G}$ G&W. $\overline{G}$ GOW are 38-73 % larger (average difference ($\overline{D}$) ~57 %) using:

$$1 - (\overline{G}_{SPLD} / \overline{G}_{GOW})$$

compared to $\overline{G}$ SPLD; whereas $\overline{G}$ G&W were only 1 to 47 % larger ($\overline{D}$~29 %) (Fig. 2.5, Table 2.1). There are several possible explanations for these differences. The most obvious explanation for the smaller $\overline{G}$ found using SPLD versus GOW is that *Gow* (1969) uses only the fifty largest grains. This also explains why the difference between $\overline{G}$ SPLD and $\overline{G}$ GOW as compared to $\overline{G}$ SPLD and $\overline{G}$ G&W is greater. There are also several less obvious reasons for the differences. First, traditional methods of grain size measurement rely on birefringence patterns to distinguish individual grains. Adjacent

12

Table 2.1. Sample depths, ages, and average grain sizes calculated using the imaging technique of *Baker and others* (2007) in combination with the measurement technique presented here (SPLD), and the methods of *Gow* (1969) (GOW), and *Gay and Weiss* (1999) (G&W). The former uses scanning electron microscope images of firn samples from the same depths (no pore filler required). The latter two methods utilize crossed-polarized photographs of thin-sections prepared using pore filler (e.g aniline or dodecane).

	Sample	Depth (m)	Age (yrs)	N	G (mm2)	σ (mm2)	Poss. Error
SPLD	02-1-16	16.335	47	60	0.507	0.206	10.85%
	02-1-32	32.339	98	88	0.569	0.278	13.47%
	02-4-12	12.918	37	80	0.166	0.084	11.26%
	02-4-18	17.938	58	45	0.272	0.125	14.07%
	02-4-42	42.878	152	66	0.3	0.182	14.82%
	02-4-46	46.853	168	51	0.367	0.191	14.61%
	02-4-60	60.16	230	59	0.619	0.306	12.88%
	02-SP-30	29.45	192	77	0.202	0.104	11.65%
	02-SP-95	94.18	853	63	0.667	0.327	12.34%
	02-SP-110	109.04	1025	55	0.571	0.328	15.53%
GOW	02-1-16	16.335	47	50	0.815	0.472	6.40%
	02-1-32	32.339	98	50	1.3408	0.661	7.40%
	02-4-12	12.918	37	50	0.3413	0.167	6.62%
	02-4-18	17.938	58	50	0.4837	0.219	5.82%
	02-4-42	42.878	152	50	1.1204	0.387	5.86%
	02-4-46	46.853	168	50	1.13	0.149	7.49%
	02-4-60	60.16	230	50	1.2265	0.560	7.57%
	02-SP-30	29.45	192	50	0.6277	0.212	4.29%
	02-SP-95	94.18	853	50	1.3239	0.538	6.72%
	02-SP-110	109.04	1025	50	2.09	0.603	9.68%
G&W	02-1-16	16.335	47	516	0.637	0.225	7.74%
	02-1-32	32.339	98	410	0.865	0.342	6.99%
	02-4-12	12.918	37	250	0.313	0.069	5.72%
	02-4-18	17.938	58	255	0.462	0.093	5.42%
	02-4-42	42.878	152	598	0.53	0.193	4.88%
	02-4-46	46.853	168	598	0.61	0.576	3.71%
	02-4-60	60.16	230	511	0.641	0.223	5.02%
	02-SP-30	29.45	192	913	0.321	0.151	6.72%
	02-SP-95	94.18	853	540	0.676	0.289	6.33%
	02-SP-110	109.04	1025	489	0.71	0.838	8.19%

grains with the same c-axis orientations will appear as one, which partially explains the larger $\overline{G}$ found for the GOW and G&W samples. In addition, automated image analysis routines often fail to identify individual grains in firn. Thus grains need to be identified

manually, a process which is time consuming and prone to operator error. These limitations are particularly true for shallow samples where the number of grains in a single thin-section is very large. Additionally, the grain boundaries are often blurred and distorted due to the use of pore fillers.

A potential correlation exists between $\overline{G}$ and/or depth and measurement technique. The reduction in grain size derived from SPLD is greatest in small grains. A cut-off grain size of 0.4 mm^2 (approximately the mean of all samples) was used to illustrate this point. $\overline{G}$ GOW is 60.7% larger than $\overline{G}$ SPLD and $\overline{G}$ G&W is 41.7% larger than $\overline{G}$ SPLD when $\overline{G}$ SPLD is < 0.4 mm^2. When $\overline{G}$ SPLD is > 0.4 mm^2, the differences decrease to 53.4% (GOW) and 15.8% (G&W). Fig. 2.5 shows the percent difference between $\overline{G}$ SPLD and both $\overline{G}$ GOW and $\overline{G}$ G&W plotted as a function of depth. Samples with $\overline{G}$ SPLD < 0.4 mm^2 have a median depth of 29.45 m; samples with $\overline{G}$ SPLD > 0.4 mm^2 have a median depth of 60.16 m. While $\overline{G}$ SPLD of both the shallow and deeper samples are smaller than $\overline{G}$ GOW and $\overline{G}$ G&W, the difference is greatest in the shallower samples. The reduction in grain size obtained from the SPLD technique is greater in small grains and at shallow depths for the following reasons: 1) Previous methods over-estimated the size of small grains by including pore filler in the grain outline. The number and size of pores decrease with increasing depth therefore, this over-estimation decreases with depth. 2) Features identified as individual grains in shallow thin-sections were probably aggregates of several grains. As grains grow larger, the birefringence within an individual grain becomes more defined and thus individual grains are more easily identified. 3) The boundaries of small, shallow grains are better defined in SEM images and consequently identified with greater accuracy.

14
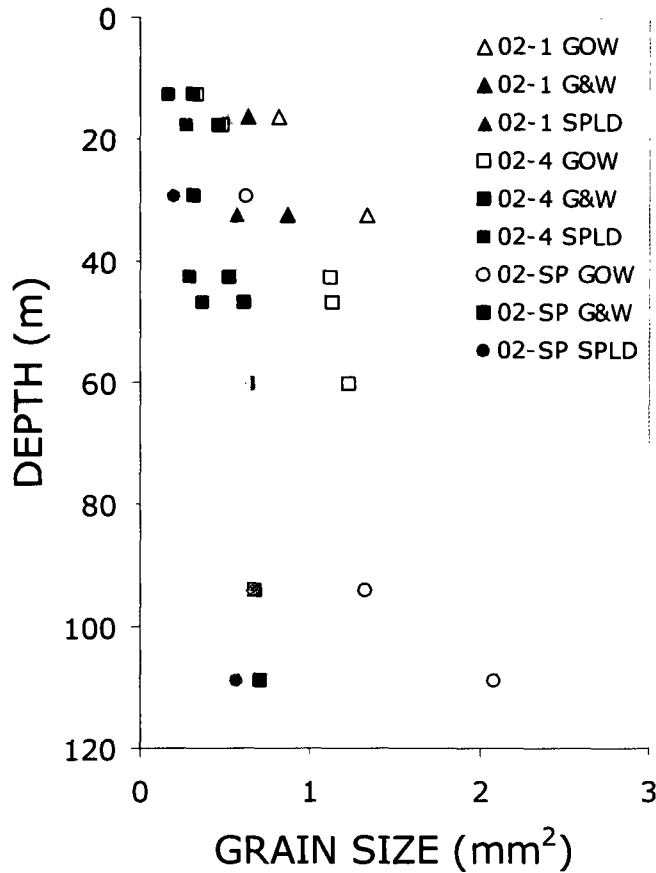
FIGURE 2.4. Grain size versus depth using three different measurement techniques. GOW average 57.1% larger than SPLD; G&W average 27.8% larger than SPLD. Data from Table 2.1.

There is a 25.9% decrease in the difference between $\overline{G}_{SPLD}$ and $\overline{G}_{G\&W}$ for grains smaller than 0.4 mm^2 and those greater than this size. For $\overline{G}_{SPLD}$ versus $\overline{G}_{GOW}$, the decrease is only 7.3% (Fig. 2.5). A paired t-test was performed to determine if the sample means above and below 0.4 mm^2 were significantly different (i.e. if the difference between techniques is really biased towards small grains). $\overline{D}_{\overline{G}_{G\&W}}$ < 0.4 mm^2 is not significantly different than $\overline{D}_{\overline{G}_{G\&W}}$ > 0.4 mm^2 (one-tail p = 0.24). Conversely, $\overline{D}_{\overline{G}_{G\&W}}$ <

15

0.4 mm^2 is significantly different than the $\overline{D}_{\overline{G}\,G\&W} > 0.4$ mm^2 (one-tail p = 0.009). The significance and magnitude of the size bias is likely greater in G&W than in GOW because *Gay and Weiss* (1999) designed their automated outlining program for use on ice, not firn. As discussed above, the use of pore fillers is more problematic in firn than in less porous ice. Thus, as the samples used in this study approach the microstructure of ice, the results derived using the techniques of *Gay and Weiss* (1999) become more consistent with those obtained using the SPLD technique. In addition, the variation in small to medium sized grains is ignored because $\overline{G}_{GOW}$ is calculated using only the 50 largest grains. Because these grains are the most difficult to measure with earlier techniques and are identified with greater accuracy using the new technique, the difference in grain size with depth between $\overline{G}$ GOW and $\overline{G}$ SPLD is expected to be dampened. If all grains were included, the size bias with depth would likely be statistically significant, as it is for $\overline{G}$ G&W.

2.3.2 Sources of Measurement Error

The calculation of grain size has several sources of potential error including the cut effect, the intersection probability effect and sample processing, as well as inconsistency in the analyst's technique (repeatability), chamber sublimation and population size. The repeatability of SEM grain size measurements was estimated using 19 samples. One area was randomly selected from an original image where the area of a number of grains equal to approximately 10% of the entire sample total (n = 4-25 grains) was determined by creating a new skeleton outline.

16
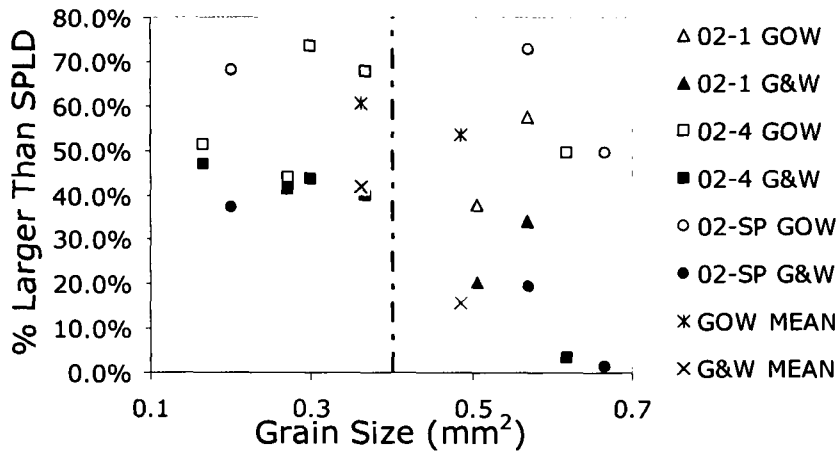
FIGURE 2.5. A potential correlation exists between size/depth and the difference in average grain size between techniques. Mean grain sizes are 60.7% (GOW) and 41.7% (G&W) larger than SPLD when $\overline{G}$ SPLD is < 0.4mm^2 and 53.4% (GOW) and 15.8% (G&W) larger when $\overline{G}$ SPLD is > 0.4mm^2.

The area of the newly outlined grains was compared to the area of the grains originally outlined to derive a repeatability standard deviation (σ_r) (*Currie*, 1995). Variance is a biased estimator of σ when the sample population (n) is small (*Montgomery and Runger*, 2003), so σ_r was multiplied by a correction factor (C_N) to remove the underestimation. Since measurements were repeated twice, n=2 and C_N is 1.2533 (*Gurland and Tripathi*, 1971). This procedure was repeated for all depths in the cores with the highest and lowest quality samples. The repeatability standard deviations for all samples were averaged to produce the single value. The decision to conduct only two trials on a large number of samples, rather than many trials on a smaller number of samples, was based on the heterogeneous quality of the samples. If many trials were performed on a single high quality sample, σ_r would be underestimated. Thus, many samples of varying quality were measured twice. The σ_r was found to be ± 0.038 mm^2 for the lowest quality core and ± 0.024 mm^2 for the highest quality core. These values were averaged to obtain the σ_r of ±

17

0.031 mm^2, with: $\overline{G}$ $_{MAX}$ = 1.036 mm^2, $\overline{G}$ $_{MIN}$ = 0.173 mm^2, and $\overline{G}$ $_{MEAN}$ = 0.435 mm^2

(Table 2.2). Thus the standard deviation is ~ 7% of the mean for the trials and the mean

of all the samples in this study ($\overline{G}$ $_{MEAN}$ = 0.424 mm^2). The measurements from the two

repeatability trials had a correlation coefficient of 0.975. Manually tracing the grain

Table 2.2. Calculation of repeatability standard deviation (*Currie*, 1995). The area of 10% of the grains in 19 samples, representing the highest and lowest quality cores, was outlined twice with more than a week in between to determine the repeatability of measurements. A correction factor (C_N) to account for the underestimation of the population standard deviation resulting from a sample size of n=2 is applied (*Gurland and Tripathi*, 1971).

Sample	Trial 1 (mm^2)	Trial 2 (mm^2)	σ_r (mm^2)	$\sigma_r{}^*C_N$ (mm^2)
062-10	0.320	0.328	0.006	0.007
062-20	0.421	0.401	0.014	0.018
062-26	0.367	0.375	0.006	0.007
062-36	0.600	0.555	0.032	0.040
062-50	0.459	0.447	0.008	0.010
062-62	0.510	0.531	0.015	0.019
062-77	0.628	0.580	0.034	0.043
062-83	0.616	0.615	0.001	0.001
062-96	1.036	0.810	0.160	0.200
074-10	0.204	0.173	0.021	0.027
074-19	0.245	0.246	0.001	0.001
074-29	0.231	0.220	0.008	0.010
074-40	0.272	0.274	0.001	0.002
074-50	0.562	0.575	0.010	0.012
074-71	0.231	0.216	0.010	0.013
074-82	0.283	0.262	0.014	0.018
074-90	0.551	0.468	0.059	0.073
074-103	0.657	0.571	0.061	0.076
074-110	0.339	0.349	0.007	0.009
			AVERAGE	**0.031**

boundaries produces the primary source of error in the repeatability calculation, thus it

can be assumed that a similar amount of error will be introduced during manual

corrections of outlines obtained using the *Gay and Weiss* (1999) technique. If the SPLD

grains are 7% larger than calculated and the G&W grains are 7% smaller, there will still

be a 30% difference in grain size between the two techniques for grain sizes smaller than

0.4mm^2. For grains larger than 0.4mm^2 measurements from SPLD and G&W may be identical, this is attributed to the increased accuracy of the SPLD technique as compared to previous techniques in the measurement of small grains.

Sublimation is known to occur in the SEM chamber (*Cullen and Baker*, 2001) and is a potential source of uncertainty in grain size measurements using SEM. If sublimation is too rapid, measured grain areas will increase or decrease during the experiment depending on where they have been sectioned (i.e. the cut effect). In order to assess repeatability, images taken at the same coordinates were compared at the beginning and the end of a session. Approximately 3.5 to 4 hours elapsed between repeat imaging. During this time, the sample was maintained in the chamber at -110 ± 5 °C. The average change in grain size over the 4 hour period was ±0.022 mm^2, corresponding to approximately 5% of the mean grain size for all samples in the repeatability test, as well as the mean grain size for all three cores in this study. The change in area during 3.5 to 4 hours of sublimation is smaller than the repeatability standard deviation. Assuming a constant sublimation rate (*Andreas*, 2007), there would only be a ±0.006 mm^2 or a 1.4 % change in $\overline{G}_{MEAN}$ during the course of normal imaging (~1 to 1.5 hours). This value is significantly less than the measure of repeatability (7%). Our analysis shows that chamber sublimation does not cause a statistically significant change in grain size during the course of normal imaging.

The effect of sample size on the reliability of SEM grain size measurements was also considered. The cold stage used to analyze firn and ice in the SEM restricts the size of the sample to a maximum dimension of 3 cm x 1 cm x 1 cm. As a result, a statistically significant population of certain grain sizes might be difficult to obtain when using only a

single sample. The possible error associated with the sample size was calculated for each type of measurement (Table 2.1) using:

$$\text{possible error} = t \times \sigma/\sqrt{n}$$

where n is the number of grains analyzed, σ is the standard deviation, and t is the one-tailed t-statistic at 95% confidence. The average possible error for SPLD is approximately twice that of both GOW and G&W. The inclusion of a larger number of grains (which was not done here) would increase the accuracy.

In a study of grain size measurements of metals and ceramics using image analysis, *Diogenes and others* (2005) report a difference of less than 2% between $\overline{G}$ calculated using approximately 1000 grains versus only 100 grains. While the averages were very similar, the standard deviations were quite different. Standard deviations associated with 100 grain size measurements were almost 2.5 times greater (40.3 % of $\overline{G}$) than those associated with 1000 grain size measurements (16.5 % of $\overline{G}$). Thus it can be assumed that average grain measurements derived from samples with few grains are indicative of the true mean, although the grain size distribution may be inaccurate. Our sample sizes were too small to obtain 100 grains per sample but this factor is not critical because our focus is quantifying $\overline{G}$ rather than grain size distribution.

2.3.3 Growth Rate

The transformation of snow to firn to ice results from increasing overburden pressure which causes a decrease in pore spacing. Angular snow grains are initially rounded through contact with one another which reduces pore space and increases density as the material becomes firn. Porosity is further reduced by sintering, the process through which material is transferred from one grain to another at initial points of contact. These

points of contact become grain boundaries. Grain boundaries are interfacial defects in the lattice of any material where there are atomic mismatches in the transition from the crystalline orientation of one grain to the next (*Callister Jr.*, 2007). In the transformation between firn and ice, there is a steady increase in grain size with depth; this normal grain growth results from a minimization of grain boundary area. Grain boundary migration is driven by the curvature of high energy grain boundaries and the stored energy difference between grains (*Burke*, 1949). Small grains are typically found on the concave side of the boundary and the pressure is typically greatest at this location. Atomic diffusion is in the direction of the low pressure location and boundary motion is in the opposite direction. Thus the grain on the high pressure side becomes incorporated into the grain on the low pressure side (*Callister Jr.*, 2007; *Sieg*, 2008) and large grains grow at the expense of smaller grains. The diffusion of molecules occurs over time and is a temperature dependent process, therefore growth rates are dependent upon depth (age) and temperature (*Paterson*, 1994).

In core 02-4, $\overline{G}_{SPLD}$ was found to increase from 0.166 mm^2 at 12.9 m (37 years) to 0.619 mm^2 at 60.2 m (230 years). Fig. 2.6 shows grain size plotted against age. A linear least-squares best fit of this data gives a rate of increase (growth rate, K) of 0.0023 mm^2 yr^{-1}. The same samples yield $\overline{G}_{GOW}$ of 0.341 mm^2 at 12.9 m, 1.226 mm^2 at 60.2 m and a K of 0.0054 mm^2 yr^{-1} (Fig. 2.6), an increase of 0.0031 mm^2 yr^{-1}. The values for G&W are $\overline{G}_{G\&W}$ of 0.313 mm^2 at 12.9 m, 0.641mm^2 at 60.2 m and a K of 0.0017 mm^2 yr^{-1}, a decrease of 0.0006 mm^2 yr^{-1} compared to K$_{SPLD}$.

In core 02-SP, $\overline{G}_{SPLD}$ increased from 0.202 mm^2 at 29.45 m (192 years) to 0.571 mm^2 at 109.04 m (1025 years), with a K of 0.0006 mm^2 yr^{-1}. The same samples yield

$\overline{G}$ GOW of 0.628 mm^2 at 29.45 m, 2.090 mm^2 at 109.04 m and a K of 0.0017 mm^2 yr^{-1}, an increase of 0.0011 mm^2 yr^{-1}. The values for G&W are $\overline{G}$ G&W of 0.321 mm^2 at 29.45 m, 0.710 mm^2 at 109.04 m and a K of 0.0005 mm^2 yr^{-1}, a decrease of 0.0001 mm^2 yr^{-1} compared to K$_{SPLD}$.

The ratio of K$_{SPLD}$ to K$_{GOW}$ is 0.426 for 02-4 and 0.353 and for 02-SP. The ratio of K$_{SPLD}$ to K$_{G\&W}$ is 1.353 for 02-4 and 1.2 for 02-SP. It is important to note that the K from 02-SP is based on 3 points, with no data between 25.5 m (192 years) and 94.1 m (853 years). The purpose of these calculations is to understand the effect of measurement technique on the slope of the T-K curve. Since the Arrhenius type dependence of this relationship was originally defined using the techniques of *Gow* (1969), only SPLD and GOW measurements are used in the calculation of activation energy; data from G&W are not considered.

2.3.4 Activation Energy

Activation energy (Ea) is calculated using the following equation:

$$E_a = -R(\partial \ln K / \partial (1/T))$$

where R is the gas constant and the remainder of the term is the slope of the T-K curve. Because grain size is dependent upon temperature, the size-biased reduction of $\overline{G}$ SPLD versus $\overline{G}$ GOW will affect the magnitude of the calculated activation energy. The validity of the SPLD method can therefore be tested using the previously defined Arrhenius type temperature dependence of grain growth (Gow, 1969; Stephenson, 1967). To be considered valid, the SPLD method must yield an Ea value consistent with the requisite ~ 6:10 ratio, as discussed above.

To calculate a new activation energy, growth rates based on grain size calculations using the SPLD method and encompassing a range of temperature regimes are required. The samples used in this study do not meet the temperature range requirements, thus new growth rates were calculated for sites previously evaluated (South Pole, Southice, Maudheim, Wilkes, and Site 2, Greenland(Figure 2.1)) in Gow (1969)[1]. The new growth rates were calculated using a correction factor based on the comparison of growth rates from the SPLD method to those of GOW. The value of the correction factor was determined by dividing the difference between the ratios of K_{SPLD}: K_{GOW} at site 02-SP and 02-4 (-0.073) by the difference in temperature between the two sites[2] (-14.0°C). The correction factor, 0.0052°C^{-1}, expresses the increase in the ratio of K_{SPLD}:K_{GOW} with each 1.0°C increase in temperature from site 02-SP. Site 02-SP was chosen as the baseline temperature because the South Polar region has the lowest mean annual surface temperatures on the continent.

The correction factor was applied to the sites from Gow (1969) using the following equation:

$$K_{SPLDX} = K_{GOWX}(0.353 - 0.0052(T_{02SP} - T_X))$$

where X is location, 0.353 is the ratio K_{SPLD}:K_{GOW} at 02-SP and T is temperature (°C). The use of this correction factor required the singular assumption that the reduction in growth rate as a function of differences in grain size measurement technique is nearly identical at sites 02-SP and South Pole. This was considered a valid assumption because both sites have similar mean annual surface temperatures and growth rates.

---

[1] Gow's original growth rates include a single data point from Greenland. The inclusion of this point is justified because the only variable in question is temperature.
[2] Temperatures for 02-SP and 02-4 were estimated using a mean annual temperature map created by D. Dixon using compile 10 m firn temperature data

The new growth rates, which changed the slope of the T-K curve from Gow's (1969) value of -5.6446 K to -6.3268 K, are shown in Fig. 2.7. The apparent activation energy subsequently changed from 46.9 kJ·mol⁻¹ to 52.6 kJ·mol⁻¹ (Fig. 2.7). Barr and Milkovich (2008) and Nasello and others (2005) reported activation energies of grain boundary diffusion of 49 kJ·mol⁻¹ and 51.1 kJ·mol⁻¹, respectively, which are similar to the value from SEM analyses. This indicates that, despite the substantial decrease in SEM-derived estimates of $\overline{G}$ and K versus those from techniques using photographs of thin sections, the resultant increase in activation energy obtained from the SPLD method still favors the assumption of an Arrhenius type dependence. However, the increase in calculated activation energy does suggest that the influence of temperature on grain growth is greater than previous indicated, as larger activation energy values indicate that more energy is required to initiate grain boundary migration.

2.4 CONCLUSION

Firn grain sizes obtained using SEM images are substantially smaller than those obtained from earlier techniques, on average 57.1% smaller than those calculated using the methods of *Gow* (1969) and 28.7% smaller than *Gay and Weiss* (1999). The SPLD technique uses clearly etched grain boundaries and the presence of open pores to identify and measure individual grains from SEM images. This approach allows for a more accurate determination of grain size, porosity, and other properties, such as those necessary to characterize firn densification (i.e. surface specific area and contact area
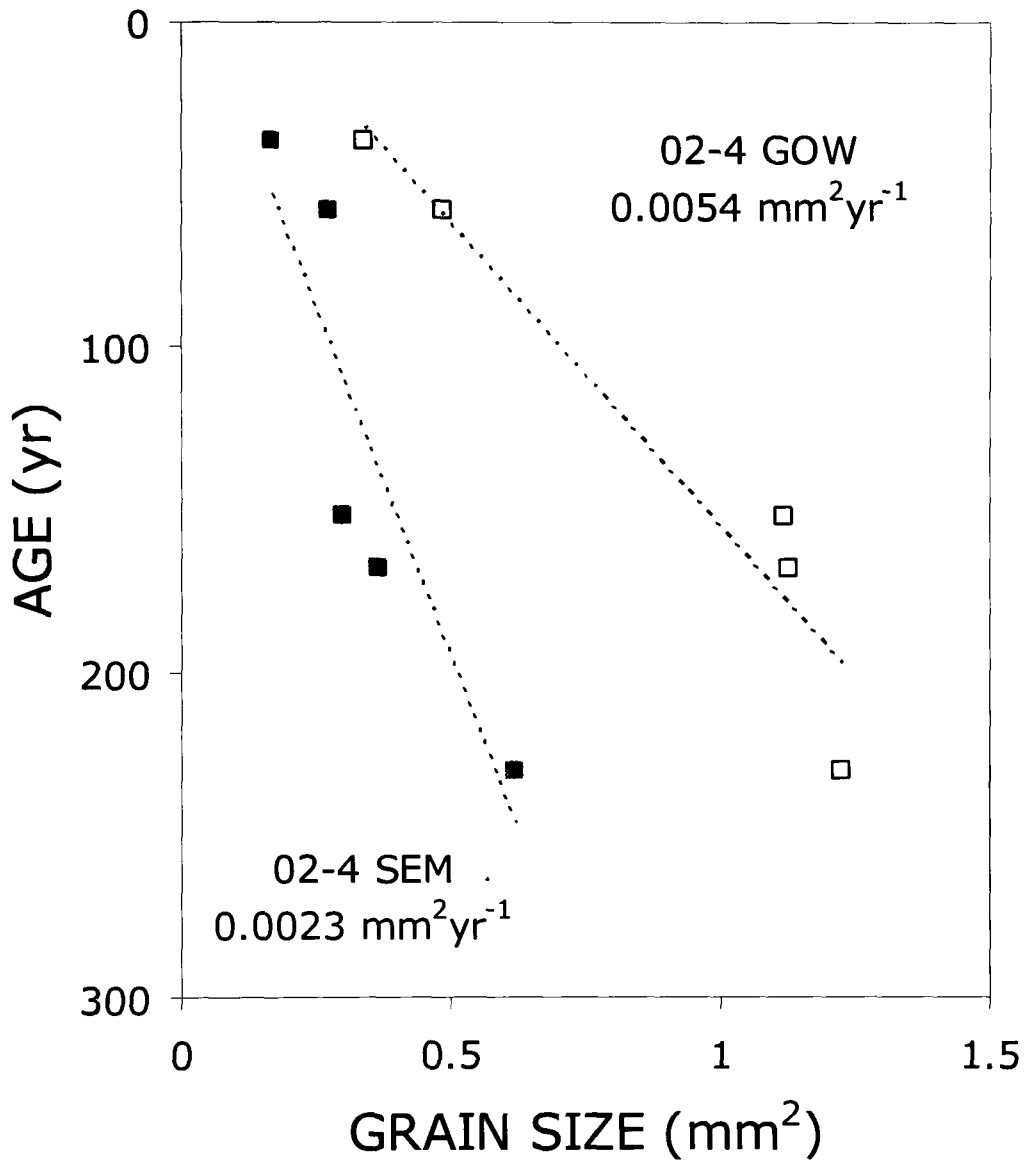
FIGURE 2.6. Determination of growth rate for 02-4 from grain sizes calculated using the technique of GOW (which along with Stephenson (1967) was originally used to define the Arrhenius type dependence) and SPLD. Data from Table 2.1.
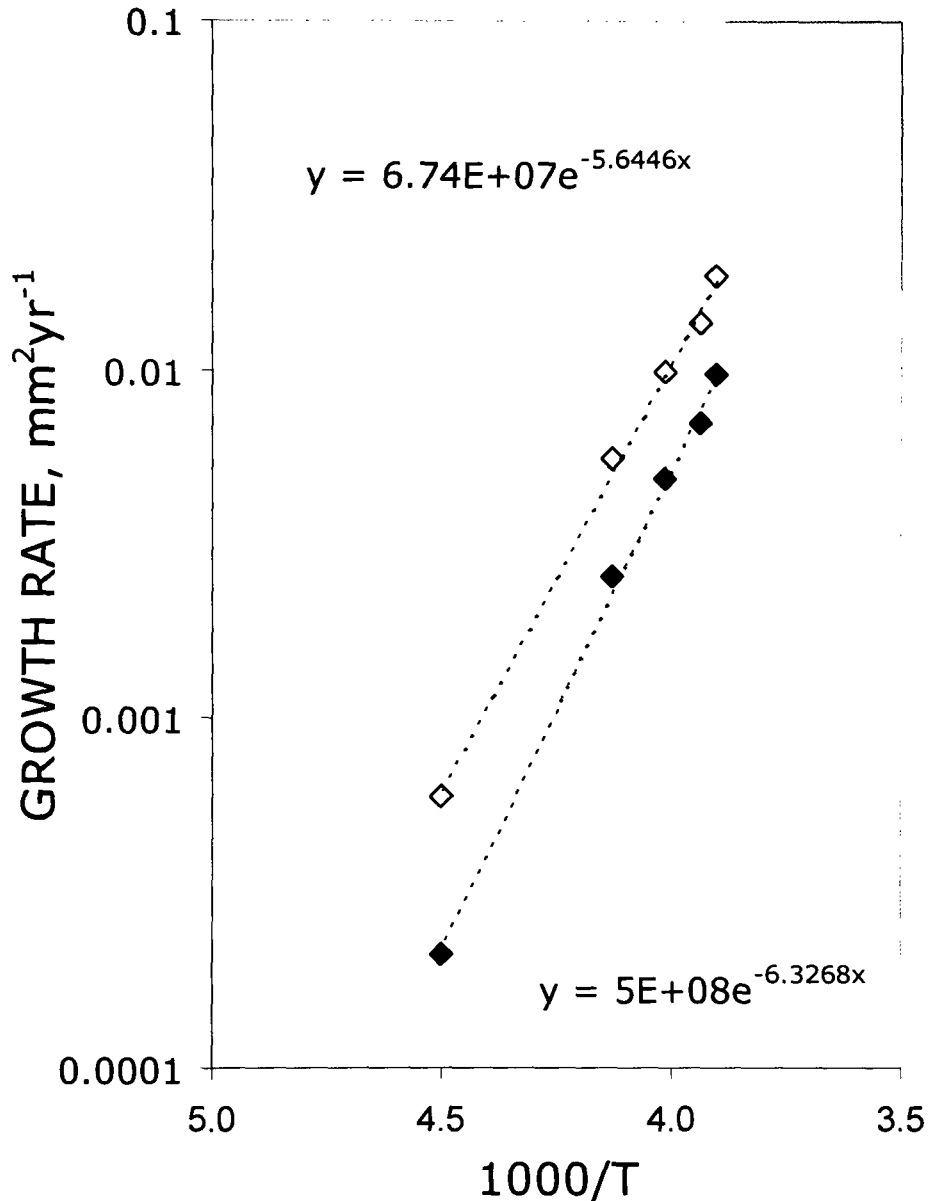
FIGURE 2.7. Grain growth rate versus reciprocal temperature calculated for five sites published in Gow (1969). Open diamonds are original data from Gow (1969). Closed diamonds show the data corrected using the calculated decrease in the ratio of K_{GOW} versus K_{SPLD} per °C increase from -51.0°C of 0.0052°C^{-1}. Activation energies of grain boundary diffusion of 49.6 kJ·mol^{-1} and 52.6 kJ·mol^{-1} are calculated from the slope.

(*Arnaud and others*, 1998)), without the need to disrupt the firn microstructure with toxic pore fillers and additional processing, as was the case with earlier methods. New grain growth rates were calculated for older core sites by applying a correction factor equivalent to the ratio of grain sizes obtained from the new technique to those from previous methods. Newly calculated grain growth rates yield an E_a of grain boundary diffusion of 52.6 kJ·mol^{-1}, similar to those from previous studies. Thus, despite the decrease in grain size, the basic relationship between grain size, growth rate, and temperature remains nearly constant. This constancy serves as a validation of the measurement technique.

The new technique presented here streamlines the collection and inter-comparison of firn and ice core microstructural data. By defining grains as single units in which visibly etched boundaries typically align with a change in axis orientation, a minimum acceptable misorientation between grains can be reported, leading to a more reliable comparison of data. This technique is especially useful for the measurement of very small grains, which are most difficult, if not impossible to measure using previous techniques. In addition, SEMs typically have associated equipment capable of determining the chemical composition of impurities within the firn and ice, therefore spatial and temporal variations in the microstructure and chemistry with depth can also be obtained. The capability to identify anomalous stratigraphic layers, study firn densification and metamorphisam, and co-register physical and chemical microstructural data will enhance the climatic interpretations of ice core proxies.

Chapter 3

CHARACTERIZATION OF FOUR EAST ANTARCTIC FIRN/ICE CORES

USING NEW IMAGING TECHNIQUES

3.1 INTRODUCTION

The microstructure of firn and ice cores, such as the size and morphology of grains, has been shown to be indicative of the physical, mechanical, and chemical characteristics of the ice sheet from which they were extracted (e.g. *Alley and others,* 1986; *Thorsteinsson and others*, 1995; *Alley and others*, 1995a, *Alley and Woods*, 1996, *Cuffey and others*, 2000). Temperature, ice flow, and impurity content can all be inferred using these properties. Thus accurate physical properties measurements are important to our understanding of ice cores as proxies for climate. More recently much attention has been given to describing the microstructural location and composition of impurities (*Cullen and Baker*, 2001; *Barnes and others*, 2002a,b; *Baker and Cullen*, 2003; *Barnes and others*, 2003; *Obbard and others*, 2003; *Barnes and Wolff*, 2004; *Baker and others*, 2005; *Iliescu and Baker*, 2008). Knowledge of these characteristics will increase our understanding of grain growth, deformation, diffusion and electrical conduction, as well as the likelihood of post-depositional interactions that may affect the reliability of climate proxies (*Kreutz and others*, 1998).

While recent work has focused on refining the methodology (*Cullen and Baker*, 2001; *Barnes and others*, 2002b; *Baker and Cullen*, 2003; *Barnes and others*, 2003; *Baker and others*, 2005; *Baker and others*, 2007) and defining and describing impurity types (*Barnes and others*, 2002a; *Obbard and others*, 2003; *Barnes and Wolff*, 2004) only limited work has been done to directly relate the morphology and microstructural location

of impurities to the physical properties they are believed to affect (*Barnes and others*, 2002a; *Iliescu and Baker*, 2008). Here, scanning electron microscopy and X-ray micro-computed tomography (micro-CT) are used to examine those relationships spatially and temporally in a suite of samples collected by the U.S. component of the International Trans-Antarctic Scientific Expedition (ITASE) .

3.2 METHODS

3.2.1 Sample Collection and Preparation

Firn and ice cores were collected during the 2006 and 2007 US ITASE traverses (Fig. 3.1) using the methodology described in *Steig and others* (2005). Samples for this study were produced by cutting a small section from one side of the 3-inch cores parallel to the vertical axis. Sub-samples were cut from these sections and the face to be analyzed was shaved with a razor blade at -20°C under a High Efficiency Particle Air (HEPA)-filtered laminar flow hood following standard clean room practices. The final specimens were flat, smooth, free of scratches, and had a maximum dimension of 0.5 cm x 1 cm x 3 cm (*Cullen and Baker*, 2001). Horizontal sections (surface analyzed is perpendicular to core axis) were taken every ten meters from all four cores (Table 3.1). Specimens were placed in a spring loaded copper sample holder, covered with a plastic cap to prevent contamination and the formation of frost on the surface and transported to the microscopy laboratory in a liquid nitrogen atmosphere.

3.2.2 Data Collection

3.2.2.1 Scanning Electron Microscopy

Samples were maintained at -110 ± 5°C in the vacuum chamber of an FEI XL30 field emission gun SEM during data collection. The SEM was operated at 15 kV with a beam current of 0.15 nA and a spot size of 3 μm. During the collection of electron backscatter diffraction patterns (EBSPs) the spot size was increased to 5 μm (*Baker and others*, 2007).
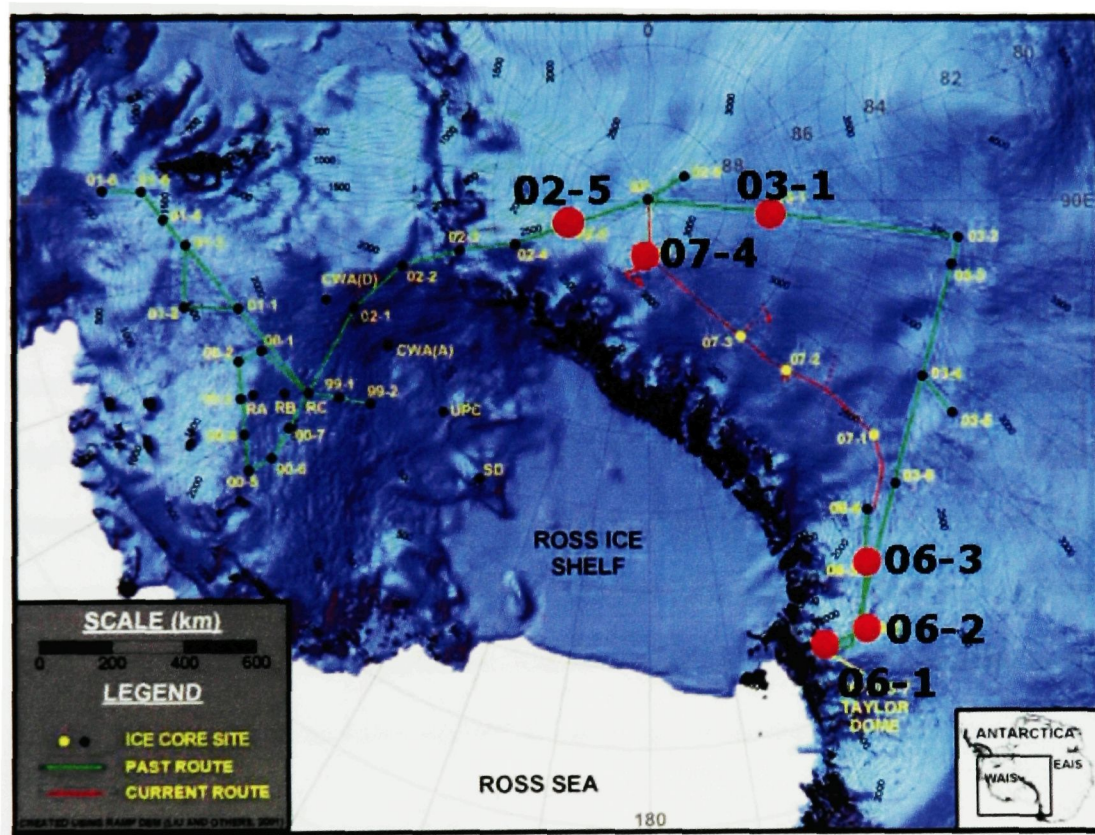
Figure 3.1. Map of core locations. 06-1, 06-2, 06-3 and 07-4 were analyzed in this study. 02-5 and 03-1 were used for comparison of EDS and IC-PMS data.

For each sample a series of slightly overlapping SEM images were collected. These images were digitally stitched together to form a mosaic of the horizontal surface of each sample.

The SEM is equipped to collect energy dispersive X-ray spectra (EDS) using an Edax light element Si(Li) detector. EDS were collected from several random locations to determine the background spectra, and additionally from triple junctions, filaments, grain boundary ridges, grain boundary grooves and crystal facets from at least 3 distinct locations per sample.

EBSPs were obtained for each core at approximately 90 m depth using an HKL, Inc. Channel 5 Orientation Imaging System (examples in Figure 3.2). Ice can be difficult to index, so numerous patterns were collected from each sample. Due to the size restrictions of the sample holder and the grain size at these depths, more than one sample was required to obtain enough patterns. At least 60 patterns from each sample were of a high enough quality to index. Imaging was performed using a forward-scatter electron detector and EBSPs were obtained by stopping the beam at a point of interest. Patterns were produced by back-scattered electrons collected on a phosphor screen and recorded using a CCD camera. The sample was held by a copper sample holder pre-titled to 10° and the stage was tilted an additional 60° to maximize backscattering yield.

3.2.2.2 Field Measurements

Bulk density (ρ) and core quality were determined for each core section immediately after retrieval in the field. Stratigraphic analysis was conducted both in the field and in the laboratory. Each section of core was placed on a light table and the
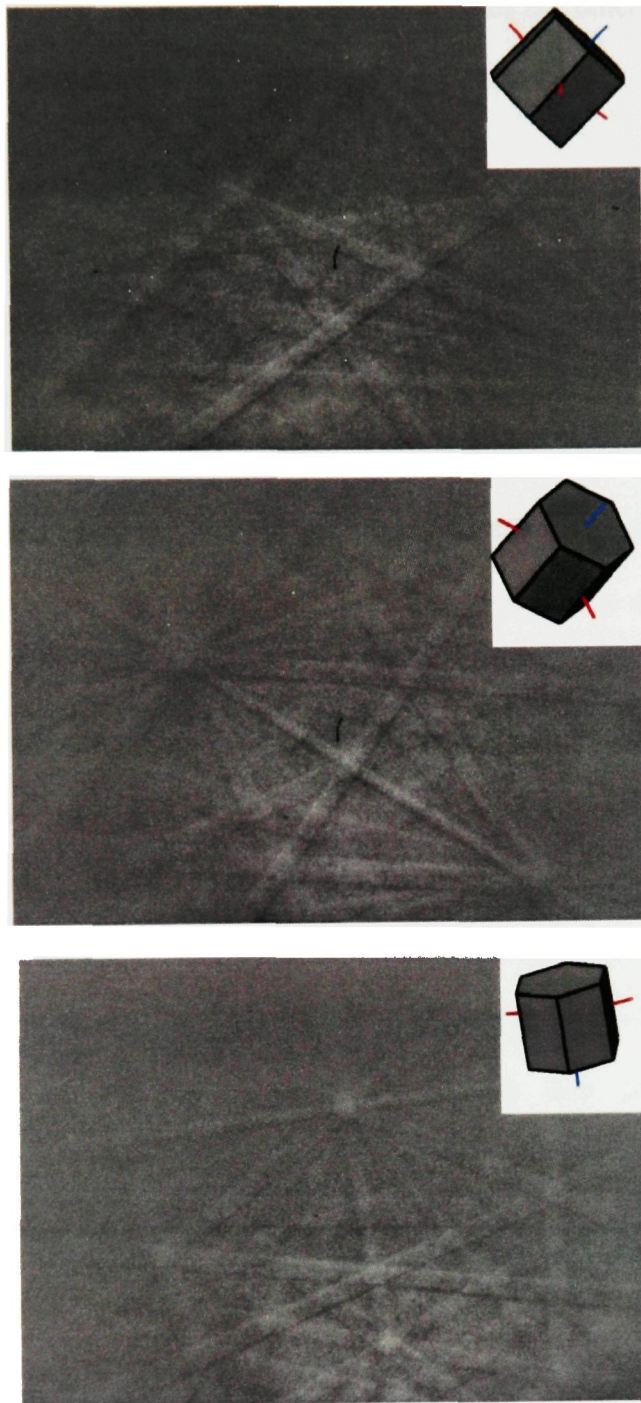
Figure 3.2. Electron backscatter diffraction patterns. Examples of patterns composed of kikuchi bands and corresponding crystal orientations.

location of coarse layers, fine layers, ice layers, wind crusts and other pertinent data were recorded at the millimeter scale.

3.2.3 Analytical Techniques

Grain sizes were determined by tracing grain boundaries on SEM images using the drawing tool in Image Pro Plus 5.0 © and then utilizing a pixel counter to determine area. For more information on this method, including repeatability, see *Spaulding and others* (submitted). Porosity was calculated as percent areal porosity by dividing the area of pores by the area of the field of view. The repeatability of porosity measurements (±1.2%) was determined by repeating the porosity determination of 10 samples from different depths.

EDS is a technique used in combination with SEM, allowing for the identification of the elements present in the observed impurities. The interaction between the electron beam and the atoms of the sample or impurity causes electrons to be ejected from the K-shell. Electrons from higher shells (e.g. L, M) move to the lower energy K-shell and release energy in the form of an X-ray photon. The emitted X-rays have a characteristic energy dependent on the type of atom from which they are produced. The "concentration" is reported as the number of x-ray counts detected. The counts can not be directly converted into a "parts per billion" type concentration for a number of reasons. First, most of the impurities found in firn and ice are light elements which produce a small number of low energy photons that are readily absorbed by the surrounding ice. The decreased production and low energy of the photons result in a low signal to noise ratio, which reduces the accuracy of the EDS system. Additionally, the strength of the X-ray current is dependent upon both the size of the impurity analyzed

(larger impurities offer a larger interaction volume) and the concentration of chemicals in the impurity. For these reasons EDS analysis of impurities is considered qualitative, rather than quantitative (*Goldstein and others*, 1992).

EBSPs were indexed to produce pole figures for the *a*-axes and *c*-axes using HKL (CHANNEL 5) pole figure and inverse pole figure software package Mambo©. Pole figures depict the orientation of each analyzed crystal as projected on the upper hemisphere of an equal area (Schmidt net) and are used to describe the fabric of the sample. The hexagonal crystal system is based on four crystallographic axes deemed a_1, a_2, a_3, and c. The three a-axes are interchangeable equatorial axes lying in the same horizontal plane. The c-axis is a line perpendicular to this plane and passing through the intersection point of the three horizontal axes. All four axes are required to describe the position of the 6 prismatic faces and 2 basal planes of the hexagon. The *c* axis points are projected on the {0001} or basal plane and the three corresponding a-axes are plotted on the {11-20} plane, which represents the face of a secondary prism within the hexagon. The pole figures were contoured using a half width of 10° (controls the spread of the pole over the surface of the project sphere) and a cluster size of 3° (replaces multiple incidents of the same orientation (i.e. from the same grain) with a single orientation point with increased weighting) to produce more easily interpretable fabric diagrams.

The misorientation angle between adjacent grains was determined using HKL (Channel 5) data management module Project Manager©. Misorientation angles describe the orientation difference between two grains in terms of the angle of rotation (about a common axis) necessary to move one crystal's coordinate system into coincidence with that of the second crystal. Hexagonal crystal systems contain twelve possible angle-axis

pairs (*Day and others*, 2004). By convention the smallest angle is referred to as the misorientation angle.

Table 3.1. Physical properties data for the firn cores used in this study. Grain size and density increase with depth, while porosity and internal surface volume (Sᵥ) decrease with depth.

Site	Identifier	Depth(m)	Density (g/cm^3)	Grain Size (mm^2)	% Porosity	S_v (mm^{-1})
2006-1	11	10.45	0.50	0.35	60	2.07
2006-1	22	20.91	0.61	0.42	43	2.23
2006-1	33	30.9	0.66	0.51	67	1.88
2006-1	43	41.53	0.69	0.61	53	2.25
2006-1	53	50.28	0.76	0.88	27	1.53
2006-1	63	60.23	0.79	0.81	21	1.35
2006-1	74	70.54	0.87	0.99	13	1.26
2006-1	85	80.28	0.88	0.98	10	0.75
2006-1	97	90.17	0.90	1.39	8	0.69
2006-2	10	10.37	0.44	0.36	64	1.85
2006-2	20	20.22	0.60	0.47	53	2.17
2006-2	26	25.87	0.60	0.40	42	2.38
2006-2	36	35.1	0.66	0.45	33	2.01
2006-2	51	50.38	0.73	0.63	31	2.19
2006-2	61	60.1	0.76	0.70	27	1.72
2006-2	77	75.24	0.74	0.95	21	1.50
2006-2	83	80.37	0.76	1.20	18	1.35
2006-2	96	90.62	0.80	1.19	12	0.86
2006-2	102	95.29	0.82	1.72	11	0.71
2006-3	10	10.05	0.52	0.25	66	2.47
2006-3	21	20.91	0.58	0.35	45	2.38
2006-3	30	30	0.64	0.61	73	1.99
2006-3	40	41.13	0.70	0.59	36	2.32
2006-3	50	50.25	0.73	0.61	27	1.98
2006-3	60	60.39	0.78	0.57	36	2.48
2006-3	70	70.01	0.78	0.84	24	1.53
2006-3	81	80.11	0.81	0.74	15	1.32
2006-3	92	90.04	0.84	0.86	18	1.33
2006-3	104	100.47	0.86		8	0.32
2007-4	10	11.45	0.51	0.16	63	2.88
2007-4	19	20.3	0.55	0.26	59	2.47
2007-4	29	30.4	0.59	0.26	69	3.62
2007-4	40	40.03	0.66	0.29	21	2.08
2007-4	50	49.31	0.67	0.57	28	1.80
2007-4	61	60.12	0.71	0.33	34	2.31
2007-4	71	70.19	0.73	0.37	35	2.09
2007-4	82	80.4	0.75	0.40	37	2.48
2007-4	92	87.89	0.78	0.58	26	1.85
2007-4	103	99.8	0.79	0.62	31	1.76
2007-4	110	106.75		0.61	20	1.26

3.3 EXPERIMENTAL RESULTS

3.3.1 Physical Properties

Fig. 3.3 shows physical properties data for all four cores used in this study plotted versus depth. As anticipated, grain size and density increase with depth while porosity and internal surface volume decrease with increasing depth. Details of grain size, density, porosity and internal surface volume (S_V) with depth are given in Table 3.1.

3.3.1.1 Grain Size

The four cores in this study exhibit a decreasing trend in grain size with distance from the coast. Core 06-1 has the highest overall grain size and is located at Taylor Dome (near the coast) whereas core 07-4 has the lowest overall grain size and is located at Titan Dome (near South Pole). The change in grain size is likely attributable to the decrease in mean annual temperature moving inland (*Bohlander and Scambos*, 2001). As expected, grain size in all cores showed a linear increase with depth (*Stephenson*, 1967; *Gow*, 1969), driven by the reduction in free energy associated with a decrease in grain boundary area.

3.3.1.2 Porosity

Core 06-2 has the lowest average porosity, with cores 06-1 and 06-3 being approximately equivalent. However, 06-1 is less porous at all depths except 30 and 40 m. Visual stratigraphy indicates that these samples were taken from a coarse layer whereas those from equivalent depths in cores 06-2 and 06-3 were taken from a fine layer, indicating differences in seasonality. If the samples from core 06-1 had been taken from a fine layer, it would likely have the lowest average porosity, in accordance with having

36

the highest overall grain size. Core 07-4 has the highest overall porosity as determined using SEM images, although it may not be significantly different from cores 06-2 or 06-3. In this core the porosity decreased from 10 to 30 m, increased from 40 to 80 m, and again decreases from 90 to 110 m. A correlation coefficient (r) between porosity and depth of 0.72 was found for 07-4 by forcing the intercept of the trendline to zero. In order to be significant at the 95% level, the r (with 9 degrees of freedom) must be at least 0.735. All other cores had an r for porosity versus depth of greater than 0.88, which was significant in every case. Core 07-4 was the only core used in this study that may have been located in one of east Antarctica's prominent megadune areas. The megadunes are areas where bedrock topography and strong katabatic winds combine to create small long wave features at the surface of the ice sheet that disrupt wind flow. Accumulating snow on the upwind side becomes fine grained and wind packed. On the downwind side, very little accumulation occurs and snow grains are exposed at the surface for several years before being buried. While at the surface, seasonal thermal cycling occurs and vapor from the crystals is released into the air in the surrounding snowpack and is then readsorbed onto the crystal, resulting in very large crystals with ample pore space. As the dunes migrate, these accumulation regimes become stacked in the ice sheet (*Courville, 2007*). The erratic porosity found in core 07-4 likely represents changes in accumulation regimes related to dune migration.

3.3.1.3 Internal Surface Volume Per Area

The internal surface volume per unit area was calculated as $S_v = (4/\pi)L_A$ where L_A is the length of the internal surface lines per unit area as determined by dividing the length of the projected surface around pores by the bounding area of those pores. S_v is a

measure of the complexity or tortuosity of the pores. Core 07-4 has the highest overall complexity while core 06-1 has the lowest. In each core S_v increases between 10 and 40-60 m and decreases between 40-60 and 100 m. *Baker and others* (2007) used samples with a depth range of 10-40 m in U.S. ITASE cores 02-SP and 02-5 and also found that S_v increased with depth, which they considered unexpected. Possible explanations for their findings include 1) increased convolution of pores despite decreased volume resulting from increased anisotropy of pore space with flattening caused by overburden pressure or 2) a side-effect of sectioning. The findings presented here indicate that S_v is initially low when each grain is an island and then increases as the grains merge and their outlines become more complex to 40-60 m. Below this depth, outlines remain consistent, but decrease in size with continued compression resulting in the decrease of S_v to values at or below original values. This shows that firn densification is not an entirely linear process, as one might expect if only porosity was considered.

3.3.1.4 Density

In addition to having the lowest porosity value and the highest degree of anisotropy of pore space, core 06-1 had the highest rate of densification of the four cores (0.0056 kg m^{-4} (i.e. kg/m^3 per meter of ice in each core section)). 07-4 had the lowest rate of densification, although the difference in the rates of densification between 06-2 (0.0037 kg m^{-4}), 06-3 (0.0039 kg m^{-4}), and 07-4 (0.0036 kg m^{-4}) were very small and may not have been statistically significant.

38

3.3.1.5 Crystallographic Orientation

The {0001} and {11-20} pole figures produced for each core at approximately 90 m are shown in Fig. 3.4. The random distribution of the points in the scatter plots suggests that the grains from all four cores have little preferred orientation. Contouring these images indicates that all the samples may have a weakly preferred c-axis orientation. The strength of the c-axis fabric was tested using the method of *Kamb* (1959), in which a coefficient f is calculated by dividing the number of c-axes in an area of the projection (A) by the standard deviation (σ) of the number of axes expected from a random distribution. Both A and σ are determined by a statistical relationship from the number of data points evaluated (N), such that when N increases, A decreases and σ increases. A value of $f \leq 3$ is expected when there is no preferred orientation. Statistically significant preferred orientations are described by $f \geq 6$. None of the fabrics analyzed here were shown to be statistically random (Table 3.2).

Table 3.2. Determination of the strength of the c-axis fabric using Kamb (1959). Variables are outlined in the text. Only 074-10 does not have a statistically significant preferred orientation.

	N	Σ	N	f
061-97	102	2.6	20	8
061-97b	76	2.5	17	7
062-96	108	2.7	25	9
063-92	77	2.5	25	10
074-90	100	2.6	19	7
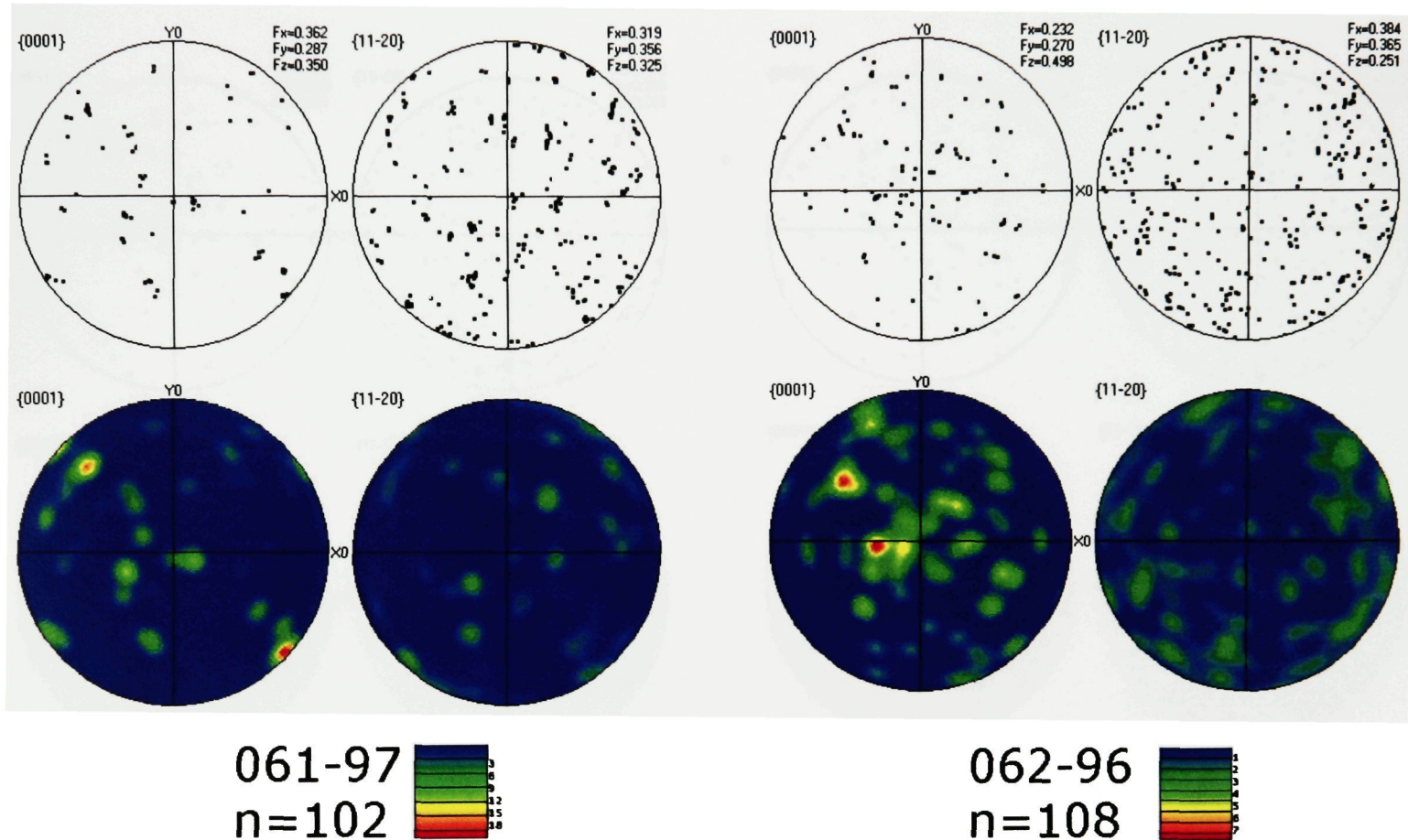
Figure 3.4. Crystallographic orientation patterns. Patterns are shown for the ~ 90 m samples. In each series the left hand circle is the c-axis {0001}plane and the right hand series are the a-axes {11-20} plane. Statistically significant preferred orientations are found in all four samples.
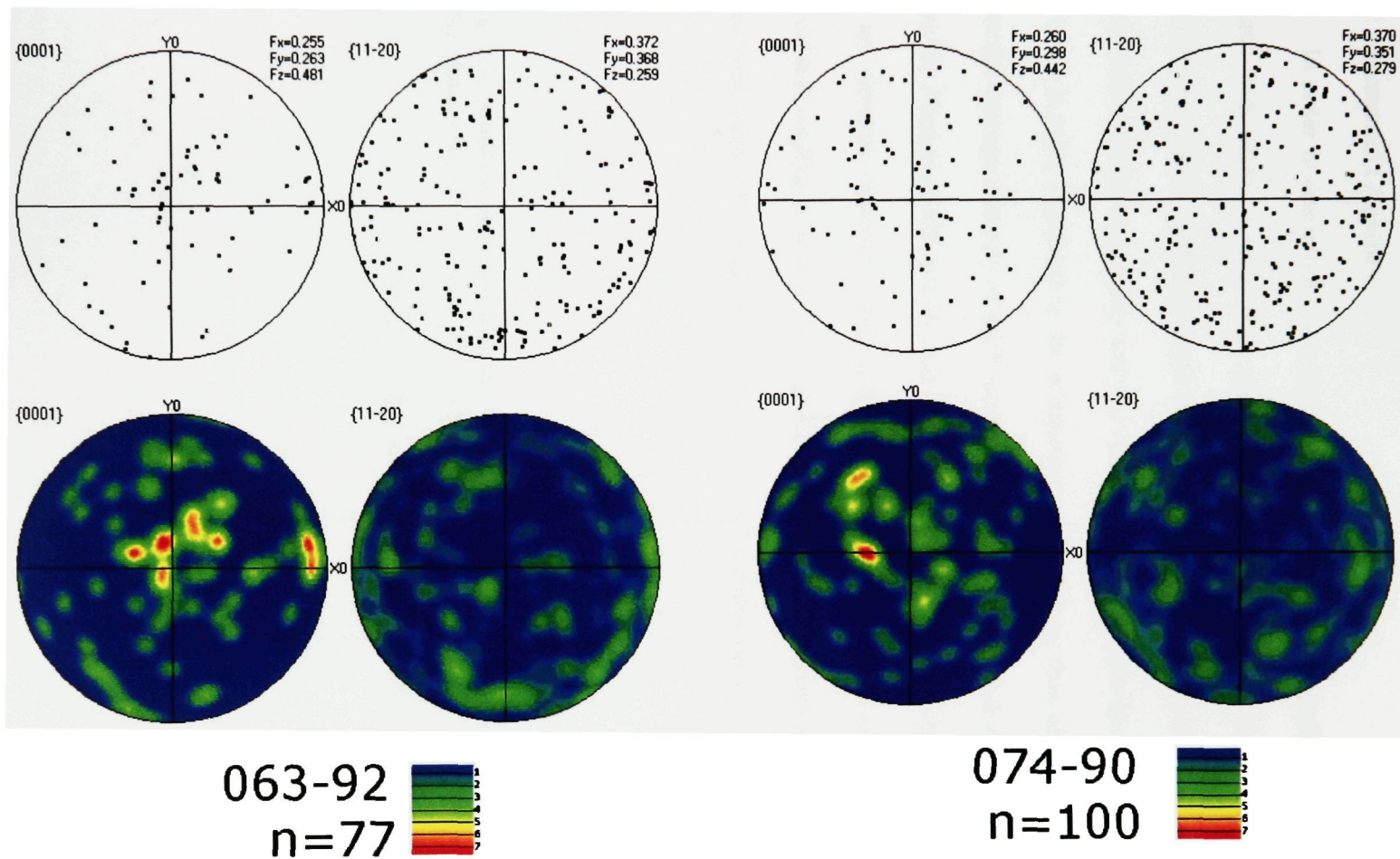
Figure 3.4. Continued…

3.3.2 Chemical Properties

3.3.2.1 Elemental Chemistry

In order to determine if the elemental chemistry or the distribution of impurities changed with depth, samples from approximately 30, 60, and 90 m in each core were analyzed using EDS. Although depth was used to identify each sample, it is important to keep in mind that the seasonality and age of the stratigraphic layer from which the sample was taken is more important to the comparison of chemistry than depth alone. Fig. 3.5 shows the average intensity of the 8 most common elements at each depth, while Fig. 3.6 shows the frequency with which each element occurred at each depth. It may be assumed that an element occurring with greater frequency contributes more greatly to the aerosol/dust loading at the time of deposition. Table 3.3 illustrates the number of points (of the total analyzed) containing elemental chemistry above background at each depth.

Table 3.3. Number of analysis points at each depth in each core. See Fig. 3.5 and 3.6 for elemental composition and frequency.

	30m	60m	90m	Total # of spectra	% with Chemistry
06-1	3	8	13	39	61.5
06-2	4	4	10	43	41.8
06-3	13	8	4	37	67.6
07-4	6	9	10	30	83.3
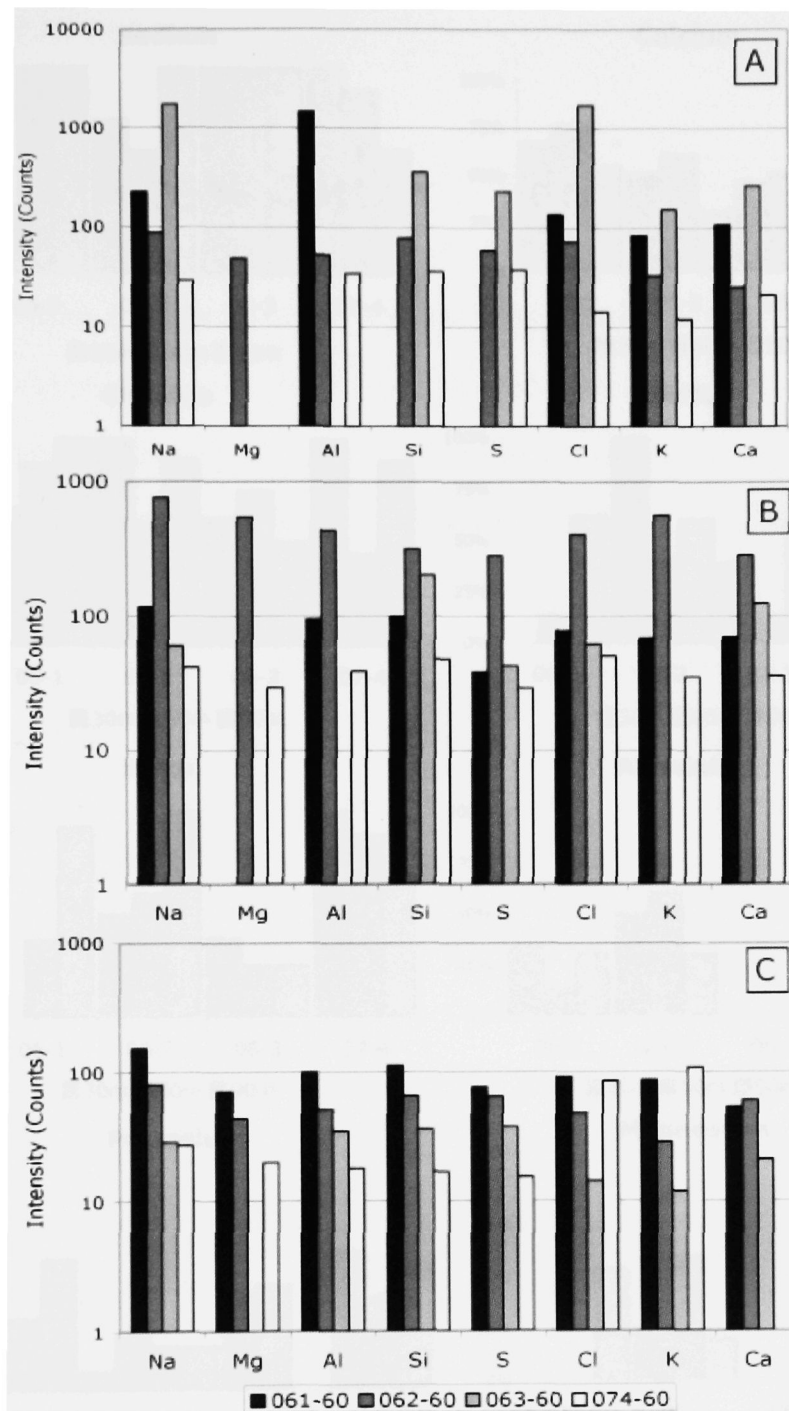
Figure 3.5. The average intensity in counts per second of the 8 most common elements at each depth. Although depth was used to identify each sample, the seasonality and age of the samples are more important for comparison of elemental chemistry. Note that in most cases the intensity [concentration] is greatest at 06-1 and lowest at 07-4.
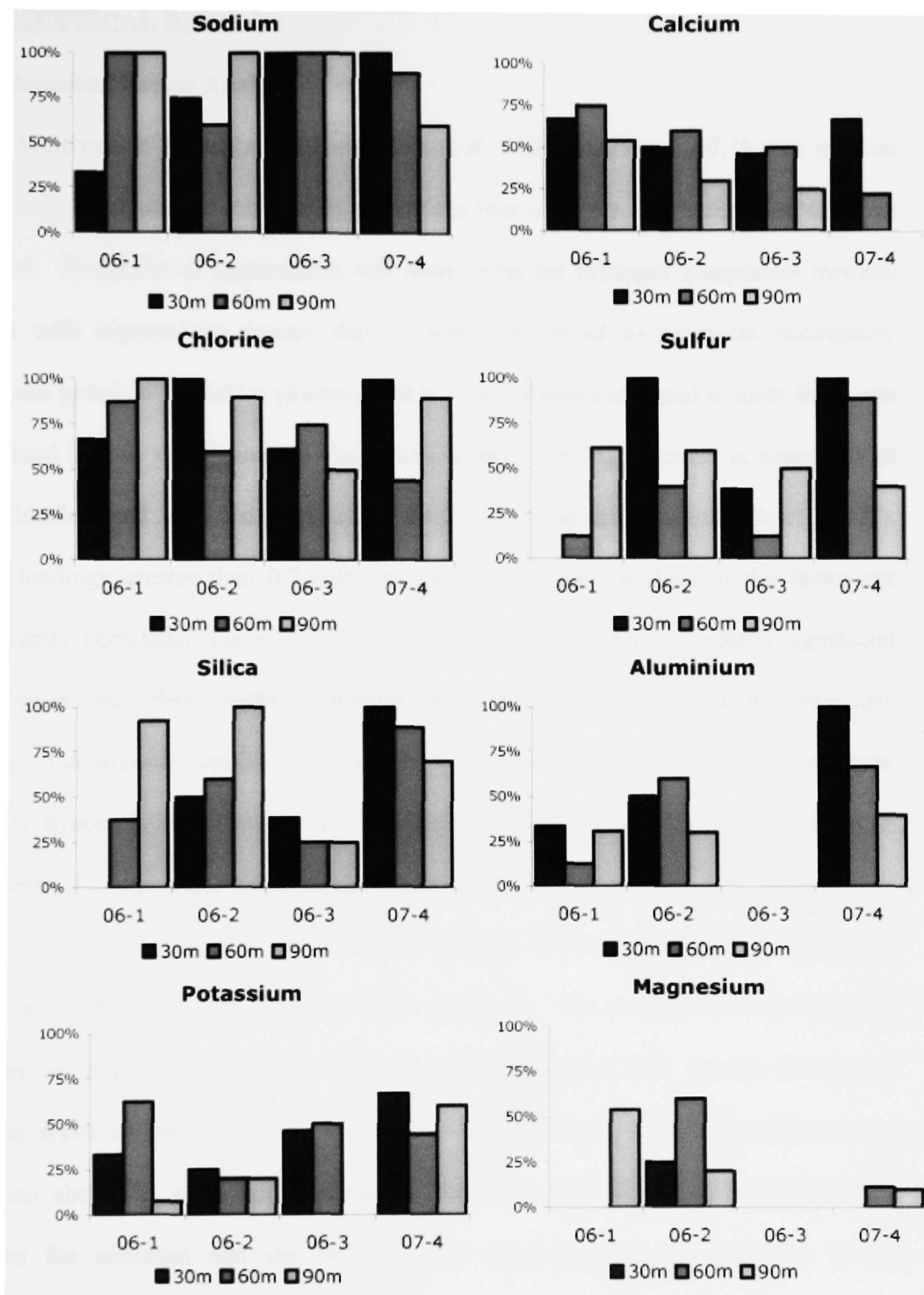
Figure 3.6. Frequency of occurrence of the 8 most common elements at each depth. Frequency is determined by dividing the number of times that element is seen by the number of spectra at that depth that contain chemistry beyond background levels.

3.4 ANALYTICAL RESULTS

3.4.1 Elemental Factor Analysis

Multivariate statistical analysis (*Robert K. Fitch*; version 2007.1) was used to examine the elemental associations in each of the four cores for which chemical data was collected. Extraction of eigenvalues was done using the principal component method. Factors with eigenvalues greater than 1 were considered to represent statistically significant groups of variables (*Kaiser*, 1960). The variables assigned to each factor are determined by the significance of their correlations. The significance is expressed as factor loading and is determined using Varimax orthogonal rotation (*Davis*, 2002). Factor loadings greater than 0.7 indicate that each of the variables in the factor are significantly correlated. Factor loadings less than 0.4 were not considered significant (*Mil-Homens and others*, 2009). Non-elemental characteristics, such as depth, grain size, porosity, and impurity structure or location were also included in the factor analysis. Impurity structures and locations are as follows: BWS: bright white spots, GB: grain boundaries, TJ: triple junctions (the intersection of three grains), ICE: background (parts of the sample which appear gray in SEM images), INC: large inclusions (insoluble impurities), TAN: filament tufts, and FIL: filaments. An example of each impurity structure or location is shown in Fig. 3.7. Representative EDS spectra for several impurity types are shown in Fig. 3.8. Factor analysis was meant to not only answer questions about the elemental associations, but also questions about the relationship between the elements and the non-elemental characteristics; for example, is the morphology or microstructural location of the impurities indicative of a particular chemical composition? Table 3.4 shows the results of all four factor analyses conducted.

3.5 DISCUSSION

3.5.1 Glaciology

The physical and chemical properties characterized above can be used to infer the flow history of the ice sheet in the immediate vicinity of each of the cores. The location of highest density clustering on the contoured images of samples from ~ 90 m depth in cores 06-3, 06-2, and 07-4 indicates a weakly preferred orientation of c-axes near the vertical (Fig. 3.4). The contoured images also suggest that the c-axis is the primary axis of rotation because clustering of points is more evident on the {0001} figure. This type of rotation and the subsequent texture is expected in areas where the primary source of strain is vertical uniaxial compression by the weight of overlying ice (*Azuma and Higashi*, 1985). With continued vertical compression and accumulated strain history these weakly preferred orientations would likely developed into broad single maximum fabrics concentrated about the vertical (*Gow and Williamson*, 1976; *Gow and others*, 1997; *Thorsteinsson and others*, 1997; *Hooke*, 2005). As illustrated by the pole figures, with the exception of core 06-1, the samples from ~ 90 m appear to have similar deformation history.

The clustering of poles seen in 06-1 suggests that some grains may have been analyzed in duplicate. To examine this possibility, the misorientation between adjacent grains was determined. The data from one grain was eliminated in each pair of adjacent grains having misorientations less than 3.0° (the analytical resolution of the instrument at the magnification used). *A, σ,* and *f* were recalculated using the new *N*. For N = 76 a statistically significant preferred c-axis orientation still exists in 06-1, although the magnitude of *f* was less than that found previously (Table 3.2- 061-97b) and some

clustering was still evident. The inclusion of so many low angle grain boundaries in a sample with so little accumulated strain history is unexpected. If the sample were from
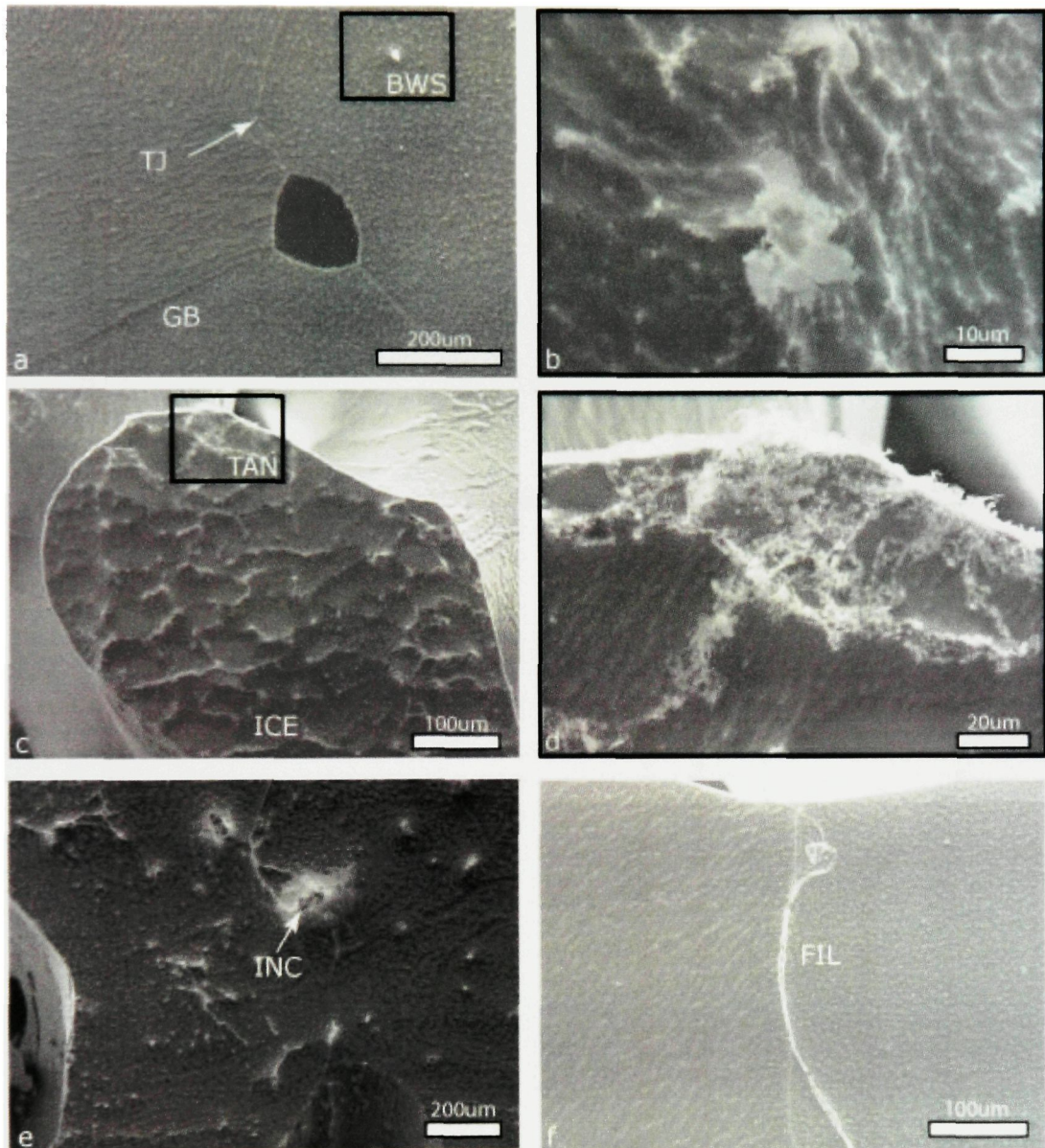
Figure 3.7. The seven impurity structures and locations analyzed are shown. A description of each structure or location is provided in the text. Magnifcation of black bounding boxes in the left images are shown in the image to the right.
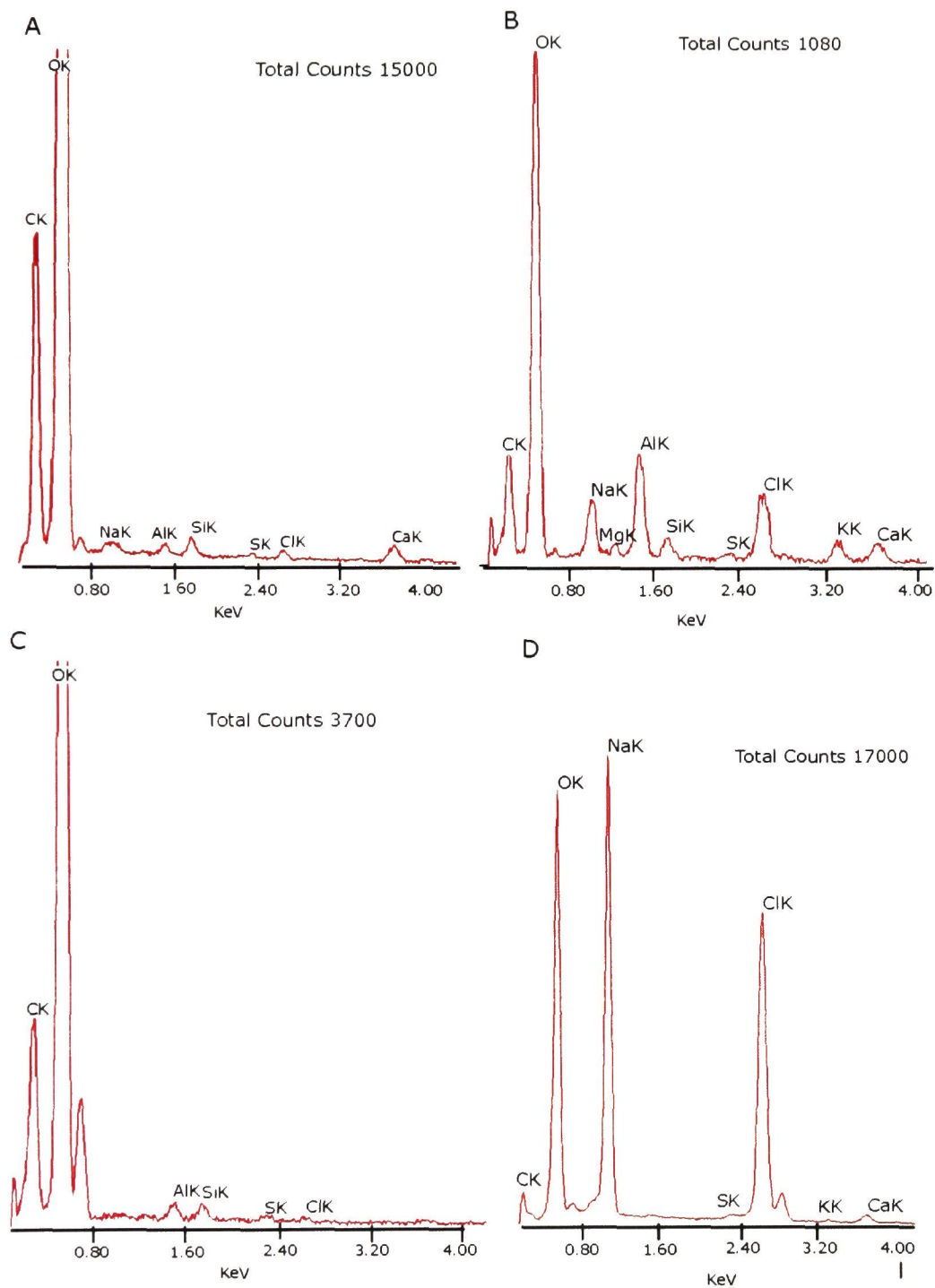
Figure 3.8. EDS spectra for common impurity morphologies. A) Bright white spot (BWS). B) Inculsion (INC). C) Filament tuft/tangle (TAN). D) Filament (FIL).

Table 3.4. Results from the factor analysis in each core. A) Core 06-1. B) Core 06-2. C) Core 06-3 and D) Core 07-4.

A	CORE 06-1		
	F1	F2	F3
Al	0.94		
Ca	0.98		
Cl			0.66
Depth	-0.97		
Grain Size	-0.97		
BWS	0.48	-0.88	
GB	-0.80	0.60	
TJ	-0.93		
ICE		0.94	
INC		0.90	
TAN	0.52	0.82	
FIL		0.96	
K		0.48	0.79
Mg	0.87		
Na	0.79		
P			
Porosity	0.81	-	-0.51
S			1.00
Si	0.96		
% of Variance	50.7	28.2	15.1

B	CORE 06-2		
	F1	F2	F3
Al	0.62	-0.53	0.58
Ca	0.98		
Cl	0.91		
Depth		0.94	
Grain Size		0.94	
BWS			0.90
GB	-0.50		-0.76
TJ		0.86	
ICE		0.43	
INC			
TAN			
FIL	0.95		
K	0.99		
Mg	0.97		
Na	0.67	-0.71	
P			
Porosity		-0.94	
S	0.90		
Si	0.63	-0.77	
% of Variance	45.17	33.30	12.60

C	CORE 06-3		
	F1	F2	F3
Al			
Ca	-0.58		0.65
Cl		0.96	
Depth	0.97		
Grain Size	0.98		
BWS			
GB			-0.68
TJ	0.97		
ICE			
INC			-0.61
TAN			
FIL		0.99	
K			0.83
Mg			
Na		0.97	
P			
Porosity	-0.95		
S	-0.72	0.67	
Si	-	0.86	-
% of Variance	33.65	29.67	14.67

D	CORE 07-4		
	F1	F2	F3
Al	-0.72		
Ca	0.71		-0.58
Cl	0.72	0.49	-0.43
Depth	0.93		
Grain Size	0.94		
BWS			0.83
GB		-0.50	-0.63
TJ			
ICE			
INC		0.78	
TAN	-0.86		
FIL	0.87		
K	0.76	0.59	
Mg		0.88	
Na			-0.77
P	0.54	-	
Porosity	-0.91		
S	-0.56		
Si	-0.86	-	-
% of Variance	45.57	16.72	16.58

50

a deeper section of the ice core, their presence could be explained by polygonization (heterogeneous deformation resulting in the organization of dislocations into subboundaries) and rotation recrystallization (boundaries become larger and the subgrains split into two distinction grains) (*Alley*, 1992; *Alley and others*, 1995b; *Durand and others*, 2008). Rotation recrystallization does not typically occur in the uppermost sections of ice sheets (*Alley*, 1992), however *Durand and others* (2008) found an over-representation of low angle grain boundaries in textures analyzed from as shallow as 115 m in the NGRIP core. Further, a study by *Hamann and others* (2004, 2005) found evidence that intra-crystalline deformation is highly inhomogenous, even close to the ice sheet surface, and showed subgrain boundaries in samples from only 104 m depth. In this study, evidence of subgrain boundaries, such as those described by *Kipfstuhl and others* (2006) was found in samples as shallow as 40 m (Fig. 3.9). Additionally, the discontinuous increase in grain size between 40 and 70 m in cores 06-1, 06-2 and 06-3 may indicate an increase in the number of low angle grain boundaries below 40 m, as low angle grain boundaries have less energy and therefore sublimate less rapidly, making the boundaries difficult or impossible to see. Given these findings it is possible that the clustering seen in the ~ 90 m sample from core 06-1 is indicative of shallow subgrain formation. These findings also suggest that shallow ice sheet metamorphism does occur and should be given consideration in ice flow modeling.

3.5.2 Chemistry

The primary sources of impurities in Antarctic ice sheets are sea salt aerosols, dust particulates, and volcanic and biogenic emissions (*Legrand and Mayewski*, 1997). *Thompson and Mosley Thompson* (1982) found that annual particulate loading decreases

as a function of the mean distance from open water, as does the accumulation rate (*Bromwich*, 1988; *Zwally and Giovinetto*, 1997). A generally decreasing trend in the concentrations of all of the eight most common elements (Fig. 3.6) between core 06-1 at Taylor Dome (~150 km from the coast) and core 07-4 at South Pole (~1300 km from the coast) was found in this study (*Bertler and others*, 2005), with the exception of K at 90 m in sample 07-4 which was greater than that of sample 06-1 at approximately 90 m. The
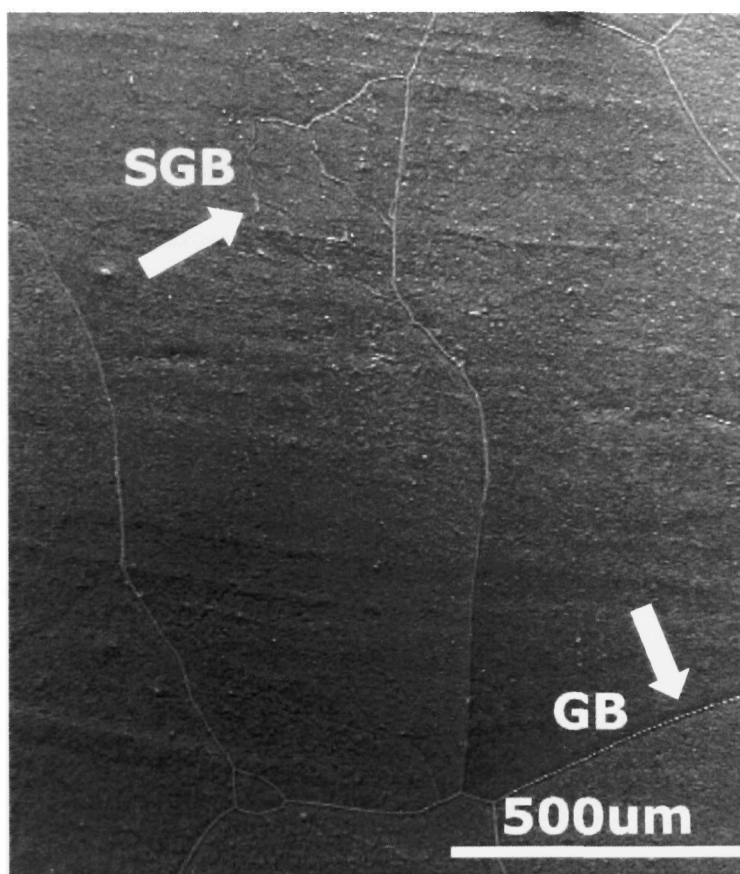

Figure 3.9. Subgrain boundaries in a sample from ~ 50 m at core site 07-1. Subgrain boundaries appear faint and kinked whereas grain boundaries are heavier and straighter.

increased concentration of K and Cl may be a byproduct of the random sampling of impurities as only one impurity analyzed in sample 06-1 at ~ 90 m contained K and with

the exception of one point of analysis all the K counts in 07-4 at ~ 90 m were lower than those in 06-1 at ~ 90 m. Differences in the seasonality of the samples analyzed at 90 m may also account for this difference.

The general trend of decreasing concentration with distance from the coastline was captured by samples in core 06-1 and 07-4, but was not seen in core 06-2 and 06-3. It is likely that in order to capture these changes on a smaller gradient (i.e. between sample sites with a smaller change in distance from the coast), more points of EDS analysis are necessary. However, this study has shown that EDS analysis is capable of accurately characterizing differences in impurity loading on a gross scale and has the potential to do so on a more macroscopic scale if higher sampling density is employed.

In addition to characterizing trends in concentration, the results of the elemental factor analysis showed that patterns of site-specific chemistry can be determined using EDS analysis as well. At Taylor Dome, the majority of Ca loading is attributed to continental dust sources and Na is attributed primarily to sea salt (*De Angelis and others*, 1997; *Legrand and Mayewski*, 1997; *Steig and others*, 2000). At South Pole, the primary source of both Ca and Na is sea salt aerosols from the ocean (*Tuncel and others*, 1989; *Legrand and Mayewski*, 1997). In core 06-1 (Taylor Dome) factor analysis found Ca loaded on F1 at the same magnitude as other continental dust elements (Al, Si). Na loaded on the same factor, but did not appear to be directly related to any other element (Table 3.4A). When factor analysis contains only elemental variables, Ca and Na are separated onto distinct factors representing the dust and sea salt contributions, respectively. The primarily continental source of Ca results from the strong southerly cyclonic systems that are the primary source of snowfall events at South Pole (*Morse and*

others, 1998). In core 07-4 (South Pole) Ca was loaded primarily with Cl indicating an oceanic source and Na was also found with Cl (Table 3.4D). Marine aerosols at South Pole are derived directly from the surrounding ocean and therefore have a shorter transit time than crustal materials, which are transported from temperate latitudes in the middle to upper troposphere (*Tuncel and others*, 1989). As a result of the decreased transit time, marine aerosols are less extensively scavenged from the atmosphere and appear more predominantly in the ice sheet (*Shaw*, 1979). Although increases in continental/dust material are seen during the austral summer, owing to the weakened temperature inversion over the polar ice cap and weakened cyclonic wind system around Antarctica, the marine source still overshadows the continental/dust input (*Legrand and Mayewski*, 1997). The findings from EDS analysis and from IC/IC-PMS analysis of other cores in the same regions record the similar trends. This shows that differences in air mass sources can be accurately determined using EDS.

At site 06-2 Na was primarily associated with dust species and Ca with marine species (Table 3.4B). At site 06-3, Na was associated only with Cl, indicating a sea salt source, while Ca was found on two separate factors associated with S on *F1* and K on *F3* (Table 3.4C). The differences in factor loadings between 06-1, 06-2, and 06-3, which all have relatively coastal locations and are in close proximity, may reflect changes in the seasonality or storm trajectories of layers sampled. Additionally, they may give some indication of the importance of site scale effects (micro-meteorology, surface topography, etc...) on deposition and post-depositional alteration.

Budner and Cole-Dai (2003) showed that South Pole ice cores record volcanic mass aerosol loading from all sources with greater fidelity than other ice cores from East

Antarctic sites with low accumulation and significant post-depositional alternation, indicating that the SO_4^{2-} record at South Pole may contain a greater contribution from volcanic aerosols than other sites. It has also been shown that greater than 95% of the SO_4^{2-} in South Pole snow originates from sources other than sea salt (*Cole-Dai and Mosley-Thompson*, 1999; *Cole-Dai and others*, 1997), with the majority being biogenic sulfate and methanesulfonic acid (MSA). Additionally, SO_4^{2-} is the dominant aerosol species in the summer at South Pole as a result of the strength of the Ross Sea/ice shelf low pressure system (*Arimoto and others*, 2004). At Taylor Dome, SO_4^{2-} is primarily related to marine biogenic sources and terrestrial biogenic and volcanic sources are less dominant (*Steig and others, 2000)*.

In Antarctic ice cores, the vast majority of S is in the form of SO_4^{-2} (*S.B. Sneed-personal communication*). This chemical configuration allows the patterns in IC SO_4^{2-} chemistry discussed above to be compared to the patterns in S chemistry as derived from EDS. In core 06-1, S loads at magnitude 1.0 on *F3* accounting for only 15.1% of the variability with only K and Cl, indicating a marine source (Table 3.4A). In core 07-4, S loads at -0.56 magnitude on F1, accounting for 45.6% of the variability. F1 also includes negative factor loadings for Al and Si (Table 3.4D). S, Si, and Al load on the same factor in core 06-2 as well (Table 3.4C). However, in that case, all elements present on F1 have positive factor loadings indicating a shared source (possibly cyclonic systems crossing the Ross Ice Shelf *(Steig and others*, 2004)); whereas in core 07-4 the loadings for Al, Si, and S are opposite in sign as compared to other elements loading on that factor indicating a different source (likely crustal materials and volcanic emissions from the mid-latitudes). The results of the factor analysis indicate variations in the sulfate loading and source, as

suggested by other techniques (i.e. potentially increased volcanic SO_4^{2-} loading in core 07-4 compared to core 06-1) can also be determined by EDS analysis of impurities.

The results of the factor analysis described above indicate that EDS analysis of impurities can provide valuable data regarding the elemental chemistry of ice core samples, including differences in air mass trajectories   More importantly these findings indicate that this type of analysis could be used to chemically fingerprint stratigraphic layers at a higher resolution than other methodologies while still allowing accurate source determination. In addition, it may be possible, using the techniques described here and a more in-depth characterization of soluble and particulate impurities, to co-register stratigraphic layers in cores from distal locations. These applications would contribute greatly to the understanding of the spatial and temporal changes in environmental conditions throughout Antarctica.

In addition to the elements shown in Fig. 3.5 and Fig. 3.6, titanium (Ti) was found in association with Al and Ca at one point of analysis in 06-1-33.   Laboratory contamination is an unlikely cause for the presence of Ti.   Instead, the Ti probably originates from dust or the products of solid rocket propellants, ablating space craft debris and interplanetary dust particles which possibly contain presolar grains and remnant condensation products from the early solar system (*Zolensky*, 1987; *Zolensky and others*, 1989). Phosphorous (P) was observed at one point of analysis in 06-3-92, in association with Si, S, and Cl and also in samples from 07-4 at 60 and 90 m, although at levels barely above background. Phosphorous derives primarily from the mineral weathering of crustal components. *Blecker and others* (2006) note that although marine deposition (from sea salt aerosols and marine biogenic PO_4 in sea ice) and eolian translocation are

possible sources of P in Antarctica (*Lancaster*, 2002; *Lyons and others*, 2003), direct atmospheric deposition is unlikely given the low levels of P in the surrounding ocean (*Stumm and Morgan*, 1981) and the limited gaseous component of the P cycle. The P seen in the samples mentioned above likely has an on continent dust source. Both Ti and P are found routinely in IC-PMS analysis of polar ice at very low concentrations.

3.5.3 Morphology and Microstructural Location of Impurities

The elements or combination of elements present determine, at least in part, the morphology and microstructural location of impurities in glacial firn/ice. The positive association found between filaments (FIL) and sea salt species indicates that filament formation requires the presence of salts (Table 3.4), which has been observed previously in filaments in snow, firn and ice (*Cullen and Baker*, 2001; *Obbard and others*, 2003; *Barnes and Wolff*, 2004; *Rosenthal and others*, 2007; *Iliescu and Baker*, 2008). The formation of filaments is believed to result from the concentration of impurities via localized surface diffusion with the sublimation of surrounding ice. Filaments are often found in grain boundaries as they are areas of high free energy and sublimate the most rapidly (*Cullen and Baker*, 2001; *Baker and Cullen*, 2003). Extended sublimation (5-8 months) has been shown to result in the formation of filaments on the bulk of the ice as well (*Rosenthal and others*, 2007). Although the samples in this study did not sublimate for an extended period of time, an intragranular filament was found encircling impurities collected at the peak of a crystal facet (Fig. 3.10). Similar to grain boundaries, the surface energy at both a facet peak and around an impurity would be greater than the surrounding ice. The presence of this intragranular filament may indicate that filaments will form wherever the concentration of impurities (resultant from localized surface

diffusion) is above a threshold value. This supports the theory that filaments are formed during sublimation and are not frozen ice veins (*Baker and Cullen*, 2008).
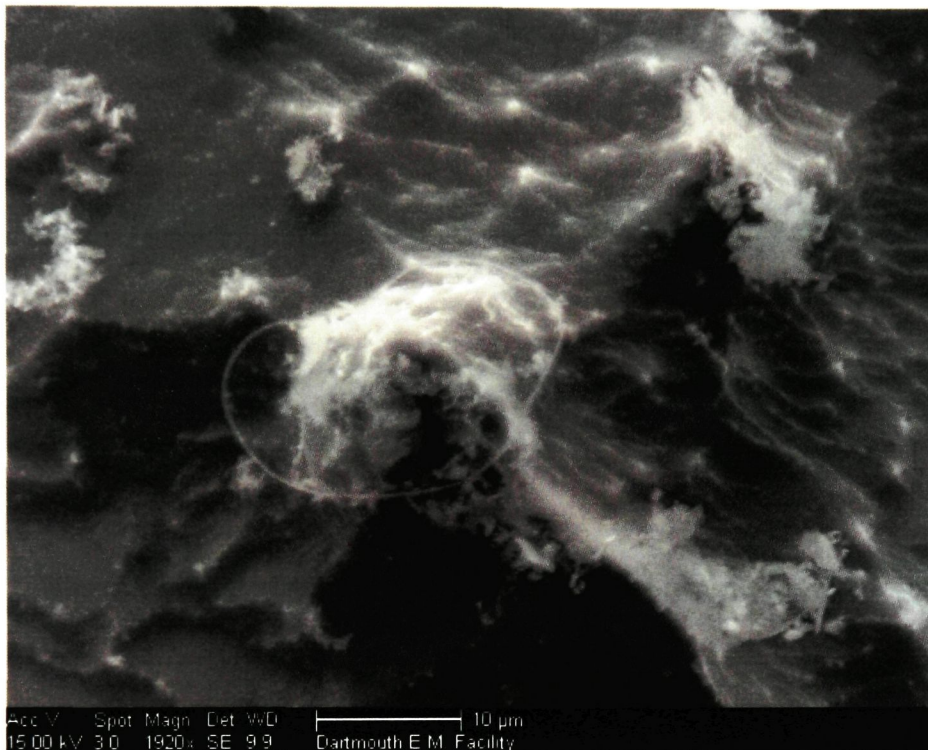
Figure 3.10. Filament around soluble impurity at facet peak from 07-4 at 11.3 m.

While the formation of filaments requires the presence of salts, the formation of filament tufts or tangles (TAN) is positively associated with the presence of dust species (Al, Si). One possible explanation for this association is that the tuft or tangle-like morphology is only possible if there is a dust particulate nucleus for the filament (formed from salt) to tangle around. *Cullen* (2000) showed SEM images of a diamond shaped inclusion (consisting of Mg and S) both before and after a nearby filament (also consisting of Mg and S) became wrapped around it. Although no such progression was captured in the study described in this paper, it provides a likely analog. *Cullen* (2000) also reported that the grain boundary filaments in the Byrd core versus those in the

GISP2 core were compositionally different, containing primarily Mg and S versus Na and Cl, respectively. Both cores had similar physical appearance, soluble lattice (intragranular) chemistry, and soluble impurity levels as determined by ion chromatography (IC), thus *Cullen* (2000) attributed the differences in filament chemistry to either the presence of non-ionic dust species (e.g. Al and Si) or to unknown environmental differences at the core sites. Filaments (FIL) observed in this study unilaterally contained Cl, while filament tufts unilaterally contained Si, but also commonly contained Cl. These chemical characterizations in conjunction with *Cullen's* (2000) photos indicate that filaments may be attracted to nearby particulates thereby forming filament tufts.

Bright white spots (BWS) are the most prevalent impurity type and previous research has shown that the BWS in a sample allowed to sublimate for a greater length of time becomes both larger and more numerous in accordance with the theory of concentration via localized surface diffusion (*Cullen and Baker*, 2001). An association between BSW and any particular element or combination of elements was not observed in this study. This lack of association may be due to incorrect categorization as a result of the limited sublimation time in the SEM chamber. It is possible that some impurities placed in this category were insoluble particulates (INC) that had not been fully exposed by sublimation, thus only appeared as bright white spots (BWS). Both dust elements (Al, Si) and marine components (Cl, S) have been reported in bright white spots (*Cullen and Baker*, 2001; *Barnes and others*, 2002a,b; *Baker and Cullen*, 2003; *Obbard and others*, 2003; *Baker and others*, 2005). *Rempel and others* (2001) found that dust particles may be coated with a liquid film in association with interfacial premelting. If the dust

particles are associated with soluble impurities, this phenomenon could also explain the lack of association between BWS and any particular set of elements.

Triple junctions (TJ) have a negative association with continental/dust species (Ca, Al, Si) in two cores and are negatively associated with Ca and S in a third. One possible explanation for this opposing relationship is that dust particles may not move into triple junctions. However, previous research has shown that soluble impurities within ice grains will be swept into grain boundaries as they migrate, particularly during recrystallization (*Glen and others*, 1977, *Iliescu and Baker*, 2008). A shear strain of ~1.15 was imparted upon the samples used in Iliescu and Baker (2008), whereas the samples used in this study were collected from a shallow part of the ice sheet and have very little accumulated strain history. The strain induced grain boundary migration in Iliescu and Baker (2008) is therefore unlikely to be consistent with the strain experienced by the samples used in this study. The lack of accumulated strain history in this study's samples means less grain boundary migration and therefore fewer opportunities for continental/dust species to be swept into the boundaries. These differences in strain history may explain why the relationship seen here is in opposition with the relationship previously reported.

Very few triple junctions (TJ) were analyzed in core 07-4 and therefore no association with dust species could be determined, however evidence of the influence of dust species on grain size was found by other means. Although the impurities analyzed in core 07-4 had the lowest concentrations of contintental/dust species (Fig. 3.5) the sampling frequency of continental/dust species (i.e., Si and Al,—Fig. 3.6) was higher than in any other core. Core 07-4 has the smallest overall grain size, given the high

continental/dust sampling frequency; it is possible that decreased grain size is a result of increased dust loading. Dust content and porosity are positively related while grain size and porosity are negatively related, indicating that in these cores, grain size is partially controlled by dust content. However, there are also several alternate explanations for the decreased grain size at site 07-4, including mean annual temperature, therefore, the relationship between grain size and dust content may be from a combination of factors or coincidental.

There were no apparent associations between any elements or combination of elements and INC (large inclusions), ICE (background) and GB (grain boundaries). Very few impurities were identified as INC and some INC may have been identified as BWS as discussed above, possibly explaining the lack of association between the characteristics examined and this impurity type. Grain boundaries placed in the GB category did not contain filaments, but rather were characterized by grain boundary ridges or grooves. Most contained no detectable elemental chemistry, however, this does not indicate there were no impurities in the grain boundaries, but rather that 1) impurity levels were below the instrumental detection limit or 2) the depth of the grain boundary groove caused the emitted x-rays to be absorbed by the surrounding ice thereby preventing detection (*Cullen and Baker*, 2001; *Barnes and others*, 2002).

3.5.4 Comparison with other Methodologies

Chemical characterization of ice cores is typically done using IC or inductively couple plasma mass spectrometry (ICMPS). Because the microstructural characterization of impurities has implications for the interpretation of IC and ICPMS data, it is important to understand the relationships between the types of measurements. For example, most

recently both of these methods have been utilized in the analysis of discrete samples collected using continuous melter systems (see *Osterberg and others*, 2006). A fraction collector is used to separate samples, which can have as high as 1 cm resolution. IC is used to measure the dissolved chemistry of major ions (Na^+, K^+, Mg^{2+}, Ca^{2+}, $CH_3SO_3^-$, Cl^-, NO_3^-. and SO_4^{2-}). IC-PMS is used to measure the trace element chemistry (e.g. ^{27}Al, ^{44}Ca, ^{56}Fe, ^{63}Cu, etc...), which requires the acidification of meltwater samples in order to dissolve particulates. IC-PMS therefore measures *total* bulk chemistry.

Previous research (Cullen, 2000) showed that despite having similar chemistry, as measured by IC, the Byrd and GISP2 cores had very different filament chemistry as determined using EDS. As discussed earlier, these differences may be attributable to the presence of non-ionic (insoluble) particulates. IC-PMS has not yet been completed on the cores used in this study, however data from two cores located to the east (03-1) and west (02-5) (unpublished, D. Dixon) of core 07-4 (Fig. 3.1) are compared.

Factor analysis of the concentrations of elements found using both EDS and IC-PMS in the three South Polar cores (Na, Ca, Mg, Al, Cl, and S) revealed site specific differences in elemental aerosol and particulate loading (Table 3.5). Core 02-5 appears to be more closely related to core 07-4 than core 03-1. Numerical simulations of the wintertime surface wind-field over Antarctica indicate that low level winds at 02-5, 03-1, and 07-4 come from the same source area (*Parish and Cassano*, 2003), however, the winds at 02-5 and 07-4 follow a more similar trajectory explaining the increased similarity in elemental chemistry between 02-5 and 07-4. The differences in factor loading between the three cores may not be related to differences in the methodology as cores 06-1, 06-2, and 06-3 were as close together as 07-4, 02-5 and 03-1 and, despite all

three (06-1, 06-2, and 06-3) having been analyzed by EDS, still exhibited differences that could be attributed to either dissimilarities in aerosol/particulate deposition or incorporation into the ice sheet owing to micro-meteorological effects.

Table 3.5. Factor Analysis of Elemental Variables in cores 07-4 (EDS) and 03-1 and 02-5 (IC-PMS).

A	CORE 07-4		B	CORE 02-5		C	CORE 03-1	
	F1	*F2*		*F1*	*F2*		*F1*	*F2*
Al	-0.44	-0.68	**Al**	-0.72		**Al**	0.87	
Ca		0.82	**Ca**		-0.74	**Ca**		
Cl		0.72	**Cl**	0.92		**Cl**	-0.46	-0.64
Mg	0.89		**Mg**			**Mg**		
Na			**Na**	0.95		**Na**	-0.77	
S	0.97	-	**S**	-0.59	0.82	**S**	-	1.00
% of Variance	32.60	28.08	***% of Variance***	46.98	22.90	***% of Variance***	28.74	26.32

Selected ratios (NaS, CaS, CaAl, NaCa, ClNa, SCl) of several common elements from both measurement types were compared. Ratios were used because it is not possible to directly compare counts to concentration. The combination of elements presented in ratios was chosen based on the correlation matrices for the three samples. Histograms of the frequency with which each of the elemental ratios occurred in the samples are presented in Fig. 3.11. Data from core 06-1 are included as well.

As illustrated in the discussion of the first factor analysis (Table 3.4) cores 06-1 and 07-4 are quite different. The relationships seen in Fig. 3.11 may indicate that the
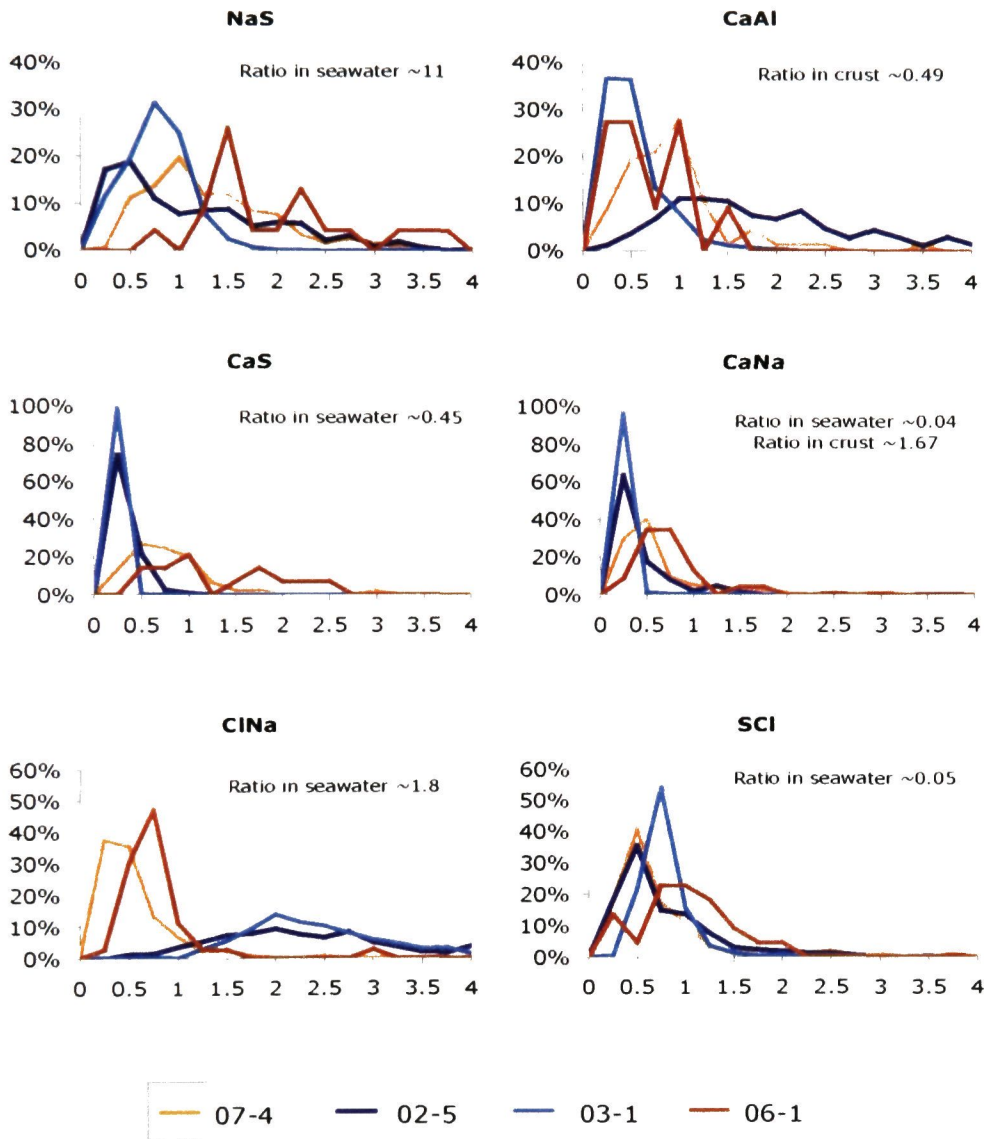
Figure 3.11. Histogram of the frequency of occurrence of elemental ratios. Ratios from EDS are shown for cores 07-4 and 06-1. 03-1 and 02-5 were analyzed using IC-PMS.

differences between EDS analysis and IC-PMS analysis render the comparison of these data impossible. However, it should be taken into consideration that EDS sampling of impurities was very random.

A more detailed centimeter by centimeter comparison of IC-PMS and EDS chemistry from core 07-4 is being completed in order to better assess the differences between EDS and IC-PMS analysis. In addition to answering these questions, those data will be used to look in more depth at the relationship between the physical and chemical characteristics within shallow firn.

3.6

3.5 CONCLUSIONS

The characterization of physical properties in four cores from the US ITASE traverses of 2006 and 2007 (06-1, 06-2, 06-3 and 07-4) revealed site-specific details that would have been missed if only chemical characterization had been completed. Erratic porosity values in core 07-4 indicate this site may be located in one of East Antarctica's vast megadunes areas. While this area has not yet been identified as such using satellite imagery, these data suggest that advanced physical properties measurements using SEM can assist in the identification of dune areas not classified as such using other methods. This capability increases the likelihood of accurately determining the quality of core sites.

Characterization of internal surface volume (S_V) at site 07-4 and others showed that the progression from firn to ice is not entirely linear, as would be assumed if only grain size or porosity were considered. Further investigation of changes in S_V with depth may aid in the understanding of the processes of firn densification and metamorphism in

the ice sheet. Both of the findings described above indicate the importance of characterizing multiple parameters to the understanding of ice cores as climate proxies.

A- and c-axis orientation data from 4 samples from approximately 90 m depth and indicated only limited preferential orientation. The c-axis is the primary axis of rotation in all four samples as a result of the overburden pressure. The high degree of clustering of poles in sample 06-1-97 and the inclusion of a great number of low angle misorientations indicate subgrain formation. Subgrains are not typically expected to form in the shallow parts of the ice sheet, however visual evidence of subgrain formation was found in samples as shallow as 50 m. These findings indicate that SEM and EBSD are valuable techniques for investigations of strain in the shallow parts of ice sheets.

The inter-regional trends in aerosol/particulate loading determined by EDS analysis of impurities are in accord with those previously published from IC and IC-PMS data. The previously established patterns of Na and Ca deposition at Taylor Dome (Ca is continental, Na is marine) and South Pole (both are marine) were accurately determined using EDS. The differences in patterns of SO_4^{2-} between the sites also indicate dissimilar SO_4^{2-} sources (i.e. volcanic versus oceanic). In addition to accurately characterizing differences in loading and incorporation into the ice sheet, EDS analysis also identified the general trend of decreasing concentration with movement inland.

The morphology and microstructural location of impurities was found to be dependent upon the elements present. As was determined in previous studies the formation of filaments (FIL) was found to require the presence of sea-salt or marine species, bright white spots (BWS) were found to contain both marine and continental

species. Not reported elsewhere is the characterization of filament tufts (TAN), which require the presence of continental (dust) species for their formation.

The analysis of both the soluble and insoluble chemistry and physical properties within a single firn or ice specimen suggests that both properties can provide valuable insights regarding environmental conditions at the time of deposition (temperature, atmospheric chemistry, atmospheric circulation patterns, etc.) and conditions affecting post-depositional alteration (micro-meteorological differences, shallow firn metamorphism, accumulation hiatuses). Many of these properties are intricately linked and investigations of their relationships using SEM, EDS, and EBSD will advance our understanding of the spatial and temporal changes in the climate of Antarctica in a way that no other instrumentation or technique could.

Chapter 4

SUMMARY

The physical and chemical characterization of firn and ice cores presented in this thesis illustrate the utility of scanning electron microscopy (SEM) and the necessity of complete characterization in the interpretation of paleoclimate proxies.

In chapter 2, a new method of grain size measurement was presented. This method utilized digital SEM images of unprocessed firn and ice samples to create a skeleton outline of the grain network from which the area of grains and pores can be calculated using a pixel counting routine. The resulting average grain size was smaller than those previously reported due, in part, to the use of pore filler which obscures the true grain size in traditional methods. The decrease in grain size was most obvious in very small grains (less than $0.4mm^2$ in size). The ability to more accurately determine grain size will aid in the identification of stratigraphic anomalies secondary to a number of environmental factors including changes in particulate loading, accumulation rate, temperature, or strain. Additional parameters can be characterized with this technique including porosity, internal surface volume, crystallographic orientation and chemical composition of impurities.

Future work in the study of grain size should involve the creation of an automated outlining program that will work with SEM images. Currently, each grain has to be manually outlined. The creation of an automated procedure will significantly decrease processing time and increase accuracy. The degree of detail captured by the SEM will make the automation of this process difficult. For example, sublimation textures can be on the same scale as grain boundaries making simple digital filtering difficult.

Automated raster to vector conversion programs created for GIS, mapping and computer automated design (Wu, 2000) could potentially be used in the development of new software.

The ability to characterize multiple parameters of a single sample was demonstrated in chapter 3 using the physical and chemical microstructure of several samples from four East Antarctic cores. This analysis yielded several unexpected results showing the importance of characterizing both chemical and physical properties. Orientation data and visual inspection of SEM images indicate the formation of subgrains shallower in the ice sheet than expected. Variable porosity values indicated possible changes in accumulation regimes suggesting that core 07-4 may be located in one of East Antarctica's vast megadunes areas. This area has not been previously identified as a megadunes area based on satellite imagery.

Site-specific differences in aerosol and particulate loading can be captured by EDS analysis. Factor analysis on the EDS spectra from site 06-1 indicated a marine Na source and a continental/dust Ca source, consistent with IC/IC-PMS analysis. Site 07-4 was found to have a primarily marine source for both Ca and Na, as indicated elsewhere for the South Polar region.

The morphology and microstructural location of impurities is determined by the elements present in the ice cores. For example, filaments, which form in rapidly sublimating areas, indicate the presence of salts; whereas filament tufts require dust elements (i.e., Al and Si) to form. This may have implications for post-depositional alteration.

This research has shown that accurate characterization of both chemical and physical properties can be achieved using scanning electron microscopy. Future research should involve a more focused and in depth comparison of the chemical and physical properties to better reveal their complex relationship. For example, mapping of impurities and misorientations may be particularly useful. In addition, a larger study including more continuous sampling and encompassing sites with more dissimilar strain history and environmental variability is suggested. Doing so will lead to a greater understanding of the relationship between the chemistry used to infer paleoenvironmental conditions and the resultant physical manifestation in ice cores.

REFERENCES

Alley, RB. 1980. Densification and recrystallization of firn at Dome C, East Antarctica. In *Institute of Polar Studies Report No. 77*. Columbus, OH: Ohio State University Institute for Polar Studies, 19-20.

Alley, RB, 1992. Flow-law hypotheses for ice-sheet modeling. *Journal of Glaciology*, **38**(129), 245–256.

Alley, RB and GA Woods. 1996. Impurity influence on normal grain growth in the GISP2 ice core, Greenland. *Journal of Glaciology*, **42**(141), 255-260.

Alley, RB, JH Perepezko and CR Bentley. 1986. Grain growth in polar ice: I. Theory. *Journal of Glaciology*, **32**(112), 415-424.

Alley, RB, AJ Gow, SJ Johnsen, J Kipfstuhl, DA Meese and T Thorsteinsson. 1995a. Comparison of deep ice cores, *Nature*, **373**, 393-394.

Alley, RB, AJ Gow, and DA Meese.1995b. Mapping c-axis fabrics to study physical processes in ice. *Journal of Glaciology*, **41**(137), 197–203.

Anderson, MP, GS Grest, and DJ Srolovitz. 1989. Computer simulation of normal grain growth in three dimensions. *Philosophical Magazine B*, **59**(3), 293-329.

Andreas, EL. 2007. New estimates for the sublimation rates for ice on the Moon. *Icarus*, **186**, 20-34.

Arnaud, L, V Lipenkov, JM Barnola, M Gay and P Duval. 1998. Modelling of the densification of polar firn: characterization of the snow-firn transition. *Annals of Glaciology*, **28**, 39-44.

Arimoto, R, A Hogan, P Grube, D Davis, J Webb, C Schloesslin, S Sage and F Raccah. 2004. Major ions and radionuclides in aerosol particles from the South Pole during ISCAT-2000. *Atmospheric Environment*, **38**, 5473-5484.

Azuma, N and A Higashi. 1985. Formation processes of ice fabric pattern in ice sheets. *Annals of Glaciology*, **6**, 130–134.

Baker, I and D Cullen. 2003. SEM/EDS observations of impurities in polar ice: artifacts or not? *Journal of Glaciology*, **49**(165), 184–190

Baker, I, D Illiescu, R Obbard, J Chang, B Bostick and C Daghlian. 2005. Microstructural characterization of ice cores. *Annals of Glaciology*, **42**, 441-444.

Baker, I, R Obbard, D Illiescu, and D Meese. 2007. Microstructural characterization of firn. *Hydrological Processes*, **21**(12), 1624-1629.

Barnes, PRF and EW Wolff. 2004. Distribution of soluble impurities in cold glacial ice. *Journal of Glaciology*, **50**(170), 311-324.

Barnes, PRF, R Mulvaney, K Robinson, and EW Wolff. 2002a. Observations of polar ice from the Holocene and glacial period using the scanning electron microscope. *Annals of Glaciology*, **35**, 559-566.

Barnes, PRF, R Mulvaney, and K Robinson. 2002b. A technique for the examination of polar ice using the scanning electron microscope. *Journal of Microscopy*, **205**, 118-124.

Barnes, PRF, E Wolff, DC Mallard, HM Mader. 2003. SEM studies of the morphology and chemistry of polar ice. *Microscopy Research and Technique*, **62**(1), 62-69.

Barr, AC and SM Milkovich. 2008. Ice grain size and the rheology of Martian polar deposits. *Icarus*, **194**, 513-518.

Bertler, N. and 54 others. 2005. Snow chemistry across Antarctica. *Annals of Glaciology*, **41**, 167-179.

Blecker, SW, JA Ippolito, JE Barrett, DH Wall, RA Virginia, and KL Norvell. 2006. Phosphorus Fractions in Soils of Taylor Valley, Antarctica, *Soil Science Society of America Journal*, **70**, 806-815

Bohlander, J and T Scambos, compilers. 2001. *THERMAP Antarctic Ice Sheet Temperature Data*. Boulder, CO: National Snow and Ice Data Center. Digital media.

Bromwich, DH. 1988. Snowfall in high southern latitudes. *Reviews of Geophysics*, **26**, 149-168.

Budner, D and J Cole-Dai. 2003. The number and magnitude of explosive volcanic eruptions between 904 and 1865 A.D.: Quantitative evidence from a new South Pole ice core, in *Volcanism and the Earth's Atmosphere*, edited by A. Robock and C. Oppenheimer, American Geophysical Union, 165-176.

Burke, JE. 1949. Some factors affecting the rate of grain growth in metals. *Transactions of the American Institute of Mining and Metallurgical Engineers*, **180**, 73.

Callister Jr, W. 2007. Dislocations and strengthening mechanisms: 7.13 Grain Growth. In *Materials Science and Engineering An Introduction*. New York, NY: John Wiley & Sons, Inc., 200.

Cole, DG, P. Feltham, and E. Gillam. 1954. On the mechanism of grain growth in metals with special reference to steel. *Proceedings of the Royal Society of London: Series B*, **67**, 131-137.

Cole-Dai, J and E Mosley-Thompson. 1999. The Pinatubo eruption in South Polar snow and its potential value to ice core paleovolcanic records. *Annals of Glaciology*, **29**: 99-105.

Cole-Dai, J, E Mosley-Thompson, and LG Thompson. 1997. Quantifying the Pinatubo signal in south polar snow. *Geophysical Research Letters*, **24**, 2679-2682.

Courville, Z. 2007. Gas diffusivity and air permeability of the firn from cold polar sites. Ph.D. dissertation, Thayer School of Engineering, Dartmouth College.

Courville, ZR, MR Albert, MA Fahnestock, LM Cathles IV, and CA Shuman. 2007. Impacts of an accumulation hiatus on the physical properties of firn at a low accumulation polar site. *Journal of Geophysical Research*, **112**(F2), F02030.

Cuffey, KM, T Thorsteinsson, and ED Waddington. 2000. A renewed argument for cystral size control on ice sheet strain rates. *Journal of Geophysical Research*, **105**(B12), 26547-26557.

Cullen, D. 2000. The structure and chemistry of polar glacier ice. *Ph.D. Thesis*, Thayer School of Engineering, Dartmouth College, Hanover, NH, 163-165.

Cullen D and I Baker. 2001. Observation of impurities in ice. *Microscopy Research and Technique*, **55**, 198-207.

Currie, LA. 1995. Nomenclature in evaluation of analytical methods including detection and quantification capabilities. *Pure and Applied Chemistry*, **67**(10), 1699-1723.

Davis, JC. 2002. *Statistics and data analysis in geology*, Wiley: New York, p. 638.

Day, A, P Trimby, K Mehnert and B Neumann. 2004. HKL Technology, Channel 5 *[user manual]*. Hobro, Denmark: 423.

De Angelis, M, JP Stephenson, M Legrand, H Clausen and C Hammer. 1997. Primary aerosol (sea salt and soil dust) deposited in Greenland ice during the last climatic cycle: Comparison with east Antarctic records. *Journal of Geophysical Research Letters*, **102**, 26681-26698.

Durand, G, A Persson, D Samyn and A Svensson. 2008. Relation between neighbouring grains in the upper part of the NorthGRIP ice core-Implications for rotation recrystallization. *Earth and Planetary Science Letters*, **265**, 666-671.

Duval, P and C Lorius. 1980. Crystal size and climatic record down to the last ice age from Antarctic ice. *Earth and Planetary Science Letters*, **48**(1), 59-64.

Fitch, RK. 2007. *WinSTAT version 2007.1* [computer software].

Gay, M and J Weiss. 1999. Automatic reconstruction of polycrystalline ice microstructure from image analysis: application to the EPICA ice core at Dome Concordia, Antarctica. *Journal of Glaciology*, **45**(151), 547-554.

Glen, JW, DR Homer, JG Paren. 1977. Water at grain boundaries:its role in the purification of temperate glacier ice, *International Association of Hydrological Sciences Publication*, **118**, 263-271.

Goldstein, JI, DE Newbury, P Echlin, DC Joy, AD Romig, Jr., CE Lyman, C Fiori, E Lifshin. 1992. *Scanning Electron Microscopy and X-ray Microanalysis: A Text for Biologists, Material Scientists, and Geologists*, 2nd Edition, Plenum Press, New York, Chapter 3.

Gow, AJ. 1969. On the rates of growth of grains and crystals in South Polar firn. *Journal of Glaciology*, **8**(53), 241-252.

Gow AJ and T Williamson. 1976. Rheological implications of the internal structure and crystal fabrics of the West Antarctic ice sheet as revealed by deep core drilling at Byrd Station. *Geological Society of America Bulletin*, **87**(12), 1665–1677.

Gow, AJ, DA Meese, RB Alley, JJ Fitzpatrick, S Anandakrishnan, GA Woods and BC Elder. 1997. Physical and structural properties of the Greenland Ice Sheet Project 2 ice core: A review. *Journal of Geophysical Research*, **102**(26), 559-575.

Gow, AJ, DA Meese, and RW Bialas. 2004. Accumulation variability, density profiles and crystal growth trends in ITASE firn and ice cores from West Antarctica. *Annals of Glaciology*, **39**, 101-109.

Gurland, J and RC Tripathi. 1971. A simple approximation for unbiased estimation of standard deviation. *The American Statistician*, **25**(4), 30-32.

Hamann, I, S Kipfstuhl and N Azuma. 2005. Sub-grain boundary features in ice cores from EDML, Antarctica, *2005 Conference of Japanese Society of Snow and Ice*, 27.9.2005-30.9.2005, Asahikawa, Japan.

Hamman, I, S Faria, S Kipfstuhl, D Grigoriev, A Lambrecht, and F Marino. 2004. Large grain boundary hierarchy in the EPICA-DML deep ice core, Antarctica. *Geophysical Research Abstracts*, **6**, 06791.

Higgins, MD. 2000. Measurement of crystal size distributions. *American Mineralogist*, **85**(9), 1105-1116.

Hooke, RLeB. 2005. *Principles of Glacier Mechanics*, 2nd Edition, Cambridge University Press: Cambridge, p. 54-63.

Iliescu, D and I Baker. 2008. Effects of impurities and their redistribution during recrystallization of ice crystals. *Journal of Glaciology.* **54**(185), 362-370.

Kaiser, H. 1960. The application of electronic computers to factor analysis. *Educational and Psychological Measurement,* **20**, 141-151.

Kamb, WB. 1959. Ice petrofabric observations from Blue Glacier, Washington, in relation to theory and experiment. *Journal of Geophysical Research,* **64**(11), 1891-1909.

Kipfstuhl, S, I Hamann, A Lambrecht, J Freitag, SH Faria, D Grigoriev and N Azuma. 2006. Microstructure mapping: a new method for imaging deformation-induced microstructural features of ice on the grain scale. *Journal of Glaciology,* **52**(178), 398-406.

Kreutz, KJ, PA Mayewski, SI Whitlow, MS Twickler. 1998. Limited migration of soluble ionic species in a Siple Dome, Antarctica, ice core. *Annals of Glaciology,* **27**, 371-377.

Lancaster, N. 2002. Flux of eolian sediment in the McMurdo Dry Valleys, Antarctica: A preliminary assessment. *Arctic Antarctic and Alpine Research,* **34**, 318–323.

Legrand, M and PA Mayewski. 1997. Glaciochemistry of polar ice cores: A review. *Reviews of Geophysics,* **35**, 219-143.

Lyons, WB, KA Welch, AG Fountain, GL Dana, BH Vaughn, and DM McKnight. 2003. Surface glaciochemistry of Taylor Valley, southern Victoria Land, Antarctica and its relationship to stream chemistry. *Hydrological Processes,* **17**, 115–130.

Mayewski, PA. 1996. Science and Implementation Plan for US ITASE "200 Years of Past Antarctic Climate and Environmental Change", A Contribution to: The International Trans-Antarctic Science Expedition (ITASE) and the West Antarctic Ice Sheet (WAIS) Initiative, Durham, NH.

Mayewski, PA, M Frezzotti, N Bertler, T van Ommen, GH Hamilton, J Jacka, B Welch, M Frey, Q Dahe, J Ren, J Simoes, M Fily, H Oerter, F Nishio, E Iasaksson, R Mulvaney, P. Holmund, V. Lipenkov, and I. Goodwin, 2006, The International Trans-Antarctic Scientific Expedition (ITASE) - An Overview, *Annals of Glaciology,* **41**, 180-185.

Mil-Homens, M, V Branco, C Lopes, C Vale, F Abrantes, W Boer and M Vicente. 2009. Using factor analysis to characterize historical trends of trace metal contamination in a sediment core from the Tagus Prodelta, Portugal. *Water Air and Soil Pollution,* **197**, 277-287.

Montgomery, DC and GC Runger. 2003. 7-2.2 Proof that S is a biased estimator of σ. In *Applied Statistics and Probability for Engineers 3rd Edition.* New York, NY: John Wiley & Sons, Inc., 224.

Morse, DL, ED Waddington and EJ Steig. 1998. Ice age storm trajectories inferred from radar stratigraphy at Taylor Dome, Antarctica. *Geophysical Research Letters*, **25**, 3383-3386.

Nasello, OB, CL Di Prinzio and PG Guzmán. 2005. Temperature dependence of "pure" ice grain boundary mobility. *Acta Materialia*, **53**, 4863-4869.

Obbard R, D Iliescu, D Cullen and I Baker. 2003. SEM/EDS comparison of polar and seasonal temperate ice. *Microscopy Research and Technique*, **62**(1), 49-61.

Obbard, R., I. Baker and K. Seig. 2006. Using electron backscatter diffraction patterns to examine recrystallization in polar ice sheets. *Journal of Glaciology*, **52**(179), 546-557.

Osterberg, EC, MJ Handley, SB Sneed, PA Mayewski, KJ Kreutz. 2006. A continuous ice core melter system with discrete sampling for major ion, trace element and stable isotope analyses, *Environmental Science and Technology*, **40**(10), 3355-3361.

Oxford Instruments PLC. 2005. Basics of EBSD. *EBSD explained.* web 7/23/2008. <www.ebsd.com>

Parish, TR and JJ Cassano. 2003. Diagnosis of the katabatic wind influence on the wintertime Antarctic surface wind field from numerical simulations. *Monthly Weather Review*, **131**, 1128-1139.

Paterson, WSB. 1994. The transformation of snow to ice. In *The Physics of Glaciers, 3rd Edition.* New York, NY: Pergamon Press, 8-78.

Rempel, AW, JS Wettlaufer, MG Worster. 2001. Interfacial premelting and the thermomolecular force: Thermodynamic buoyancy. *Physical Review Letters*, **87**(8), 088501.

Rick, UK and MR Albert. 2004. Microstructure and permeability in the near-surface firn near a potential US deep-drilling site in West Antarctica. *Annals of Glaciology*, **39**, 62-66.

Rosenthal, W, J Saleta and J Dozier. 2007. Scanning electron microscopy of impurity structures in snow. *Cold Regions Science and Technology*, **47**, 80-89.

Shaw, GE. 1979. Abundance of chemical elements in the continental crust: A new table. *Geochimica Cosmochimica Acta*, **28**, 1983.

Sieg, K. 2008. Examination of the fine-grained region of the Siple Dome ice core. Unpublished Master's thesis, Thayer School of Engineering, Dartmouth College.

Skyscan N.V. 2005. Desktop x-ray microtomograph *[instruction manual].* Aartselaar, Belguim: 12.

Spaulding, NE, DA Meese, I Baker, PA Mayewski, and GH Hamilton. 2009. A new technique for firn grain size measurement. *Journal of Glaciology*, submitted.

Steig EJ, DL Morse, ED Waddington, M Stuiver, PM Grootes, PM Mayewski, SI Whitlow, and MS Twickler. 2000. Wisconsinan and Holocene climate history from an ice core at Taylor Dome, western Ross Embayment, Antarctica. *Geografiska Annaler*, **82A**: 213-235.

Steig EJ, PA Mayewski, DA Dixon, MM Frey, SD Kaspari, DP Schneider, SA Arcone, GS Hamilton, VB Spikes, M Albert, D Meese, AJ Gow, CA Shuman, JWC White, S Sneed, J Flaherty, M Wumkes. 2005. High-resolution ice cores from US ITASE (West Antarctica); development and validation of chronologies and estimate of precision and accuracy. *Annals of Glaciology*, **41**, 77-84.

Stephenson, PJ. 1967. Some considerations of snow metamorphism in the Antarctic ice sheet in the light of crystal studies. In H. Oura, ed. *Physics of Snow and Ice*. Institute of Low Temperature Science, 725-740.

Stumm, W, and JJ Morgan. 1981. *Aquatic chemistry: An introduction emphasizing chemical equilibria in natural waters*. 2nd ed. Wiley-Interscience. New York.

Surdyk, S. 2002. Low microwave brightness temperatures in central Antarctica: observed features and implications. *Annals of Glaciology*, **34**, 134-140.

Thompson, LG and E Mosley-Thompson. 1982. Spatial distribution of microparticles within Antarctic snow-fall. *Annals of Glaciology*, **3**, 300-306.

Thorsteinsson, T, J Kipfstuhl, J Eicken, J Johnsen and K Fuhrer. 1995. Crystal size variations in Eemian-age ice from the GRIP ice core, central Greenland. *Earth and Planetary Science Letters*, **131**(3/4), 391-394.

Thorsteinsson, T, J Kipfsthul, H Miller. 1997. Textures and fabrics in the GRIP project. *Journal of Geophysical Research*, **102** (C12), 26583–26599.

Tuncel, G, NK Aras and WH Zoller. 1989. Temporal variations and sources of elements in the south pole atmosphere 1. Nonenriched and moderately enriched elements. *Journal of Geophysical Research*, **94**(D10), 13025-13038.

Zolensky, ME, A Pun, and KL Thomas. 1989. Titanium carbide and titania phases in Antarctic ice particles of probable extraterrestrial origin. *Proceedings of the 19th Lunar and Planetary Science Conference*, Cambridge: Cambridge University Press, 505-511.

Zolensky, ME. 1987. Refractory interplanetary dust particles. *Science*, **237**(4821), 1466-1468.

BIOGRAPHY OF THE AUTHOR

Nicole Spaulding was born Nicole West in Lebanon, New Hampshire on June 8, 1984. She was raised in Hartland, Vermont and graduated from Hartford High School in 2002. She attended Colgate University and graduated magna cum laude with an Honors degree (B.A.) in Geology in May of 2006. She married Jeffry P. Spaulding on July 22, 2006 and immediately moved to Orono, ME to attend the University of Maine.

After receiving her degree, Nicole will pursue a Ph.D. in Earth Sciences at the University of Maine. Nicole is a candidate for the Master of Science degree in Quaternary and Climate Studies from the University of Maine in August, 2009.